Nanoscale

PAPER

View Article Online
View Journal | View Issue

Cite this: *Nanoscale*, 2025, **17**, 12963

Fast and accurate characterization of bioconjugated particles and solvent properties by a general nonlinear analytical relationship for the AC magnetic hysteresis area†

Pablo Palacios-Alonso,*[a,b] Mohamed M. Shams,[b] Sedef Ozel-Okcu,[b,c] Elena Sanz-de Diego,[b] F. J. Teran[b,d] and Rafael Delgado-Buscalioni*[a,e]

Brownian magnetic nanoparticles present a large sensitivity to AC fields, opening new routes to biosensing using bio-functionalized nanoparticles. The integration of theory and experiment permits the transduction of any magnetic response (*via* susceptibility, harmonics or hysteresis area) to extract relevant system's parameters (such as particle size, solvent viscosity, and temperature). Parameter estimators based on linear response theory are easy to implement, but their sensitivity and resolution are limited by construction. Nonlinear responses allow for much higher sensitivities, but demand a significant cost in complex simulations to fit the experiments, because no analytical relationship is available. Here we have solved this dilemma by deriving an empirical analytical relationship for the magnetic hysteresis area which is valid under the arbitrary field intensity and frequency, thus avoiding the need for calibration. This universal relationship matches within 1% of the outcome of the nonlinear Fokker–Planck equation and has been validated against detailed Brownian dynamic simulations and controlled experiments. Using this nonlinear magnetic hysteresis area relationship, we have built an extremely fast automated searching algorithm that simultaneously estimates several system parameters by fitting experimental data for the area (at varying intensities and frequencies). The searching scheme starts with a robust and flexible stochastic method (parallel tempering Monte Carlo) followed by an accurate deterministic multi-variable minimization (Gauss–Newton) to match experimental areas within ~1% deviation. This integrated approach upgrades AC-magnetometry into a stand-alone technique able to determine, with outstanding accuracy, particle size, polydispersity, concentration, and magnetic moment, as well as solvent viscosity and temperature. We validated this method in biosensing protocols by determining nanometer-size variations in bio-functionalized nanoparticles upon protein target recognition.

Received 10th February 2025,
Accepted 9th April 2025

DOI: 10.1039/d5nr00602c

rsc.li/nanoscale

Introduction

The need for adaptable, accurate and sensitive diagnostic assays and biomarker detection tools has significantly increased in recent times. The key is to achieve a precise transduction of some measurable physicochemical signals into relevant biomolecular properties. Nanoparticles can now achieve this goal by placing specific receptors onto their surface to capture target biomolecules. The transduction mechanism should be thus highly dependent on their size, which will slightly increase upon any capture events. This makes the magnetic moment response dominated by Brownian rotational diffusion a perfect candidate for transduction. For any nanoscale phenomena, Brownian motion is the ultimate expression of the underlying molecular randomness. However, paradoxically, stochasticity expresses itself with an outstanding precision when the system is forced to respond to periodic oscillations. Although free diffusion is associated with dispersion, under oscillatory forcing, a phase shift between the force and the system response is created by diffusion or friction, which is the basis of many accurate techniques.[1,2] Such an imperfect synchronization in energy transfer produces heat and a paradigmatic example is the AC magnetic hysteresis area observed when exposing magnetic nanoparticles (MNPs) to alternating magnetic fields (AMFs)

[a]*Dpto. Física Teórica de la Materia Condensada, Universidad Autónoma de Madrid, Madrid, 28049, Spain. E-mail: pablo.palaciosa@uam.es, rafael.delgado@uam.es*
[b]*iMdea Nanociencia, Campus Universitario de Cantoblanco, 28049 Madrid, Spain*
[c]*Nanotech Solutions S.L., Carretera. Madrid 23, 40150 Villacastin, Spain*
[d]*Nanobiotecnología (iMdea-Nanociencia), Unidad Asociada al Centro Nacional de Biotecnología (CSIC), 28049 Madrid, Spain*
[e]*Condensed Matter Institute, IFIMAC, Madrid, 28049, Spain*
† Electronic supplementary information (ESI) available. See DOI: https://doi.org/10.1039/d5nr00602c

(Fig. 1). The heat produced by lagging-behind oscillatory MNPs is the basis of hyperthermia applications, such as solid cancer treatments[3–5] or heating mediators for drug delivery systems.[6,7] Besides, since the last 20 years, MNPs have been also used in catalysis,[8] environmental[9] or biomedical applications,[10] acting as imaging agents[11–14] or transducers for biosensing technologies.[15–22] The so-called Néel-type relaxation has so far attracted most of the investigations, particularly in hyperthermia applications.[23] This relaxation mechanism is inherently magnetic as it involves thermal switching of the particle magnetic moment across its magnetic anisotropy axis, with average waiting times increasing exponentially with the anisotropy constant and the particle volume. In contrast, the relaxation of ferromagnetic MNPs (with blocked magnetic moment) is dominated by rotational diffusion. The angular diffusion of a particle of radius r_h in a fluid with viscosity η and temperature T is half the inverse of a time, $\tau_B = 4\pi\eta r_h^3/(k_B T)$, which involves both particle and medium properties. This fact is extremely useful for biosensing applications, as it could lead to accurate, multipurpose characterization tools. The idea is now recently receiving a great deal of attention[22] with most methods based on the analysis of the complex magnetization signal details (the harmonics).[24]

Here, we rather deployed the AC magnetic hysteresis area to prove and validate a method for fast and accurate characterization of particles and solvent properties. The motto driving the present theoretical and experimental efforts is the exceptional sensitivity of the MNP response under an AMF (in general) and its AC magnetic hysteresis area (in particular), which is able to detect few nanometer variations in the size of biofunctionalized particles upon protein capture.[22] This great sensitivity has multiple origins. Rotational diffusion $D_r = 1/(2\tau_B)$ scales as the inverse particle volume r_h^{-3}, which is three times more sensitive to size (in relative variation $d \ln D_r/dr_h$) than the translational one $D_t \sim r_h^{-1}$ used by techniques such as dynamic light scattering (DLS)[25] or nanoparticle tracking analysis (NTA).[26] Moreover, AMF samples phase-lag at kHz rates, while DLS and NTA samples slow random motions and require very low concentrations,[27,28] often overestimating the particle size.[29] It comes as no surprise that our AMF-based measurements improve DLS and NTA measurements, both in accuracy and precision. This benefit is also present in other AMF-based techniques, notably in alternating current susceptometry (ACS) which is usually combined with the analytical relationships provided by linear response theory (LRT)[15–17,30] (dating back to the Debye model[31]) to transduce AMF signals into particle sizes.[32–38] However, ACS-LRT cannot benefit from two key properties offered by transducers working under non-linear response.[20–22,39–41] First, while linear equations have a single solution and are fitted with a single parameter, non-linearity allows for multiple and simultaneous measurements (channels). Second, as we prove later on, the maximum area sensitivity against any system properties (again variation in the

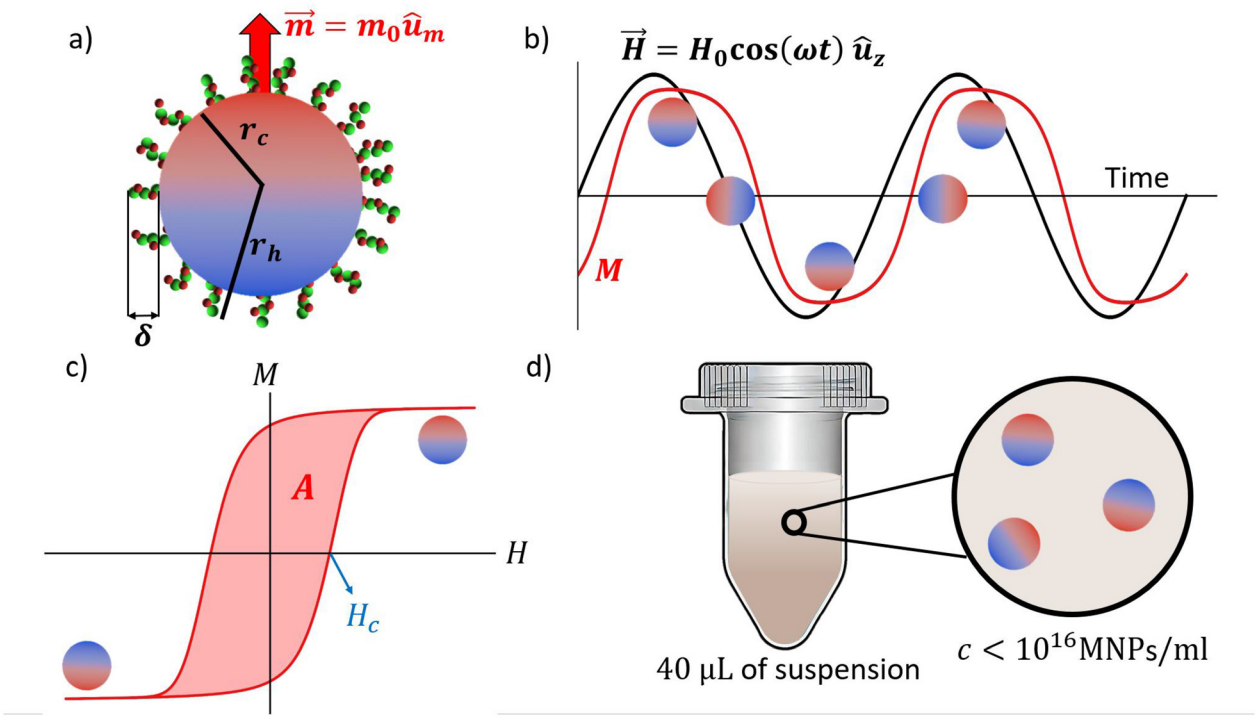

Fig. 1 (a) Schematic of the system under study, individual MNPs with the magnetic moment blocked that might be coated with some biomolecules. (b) Example of the variation of the magnetic field (black) and the magnetization of the system in the z direction (red) as a function of time for arbitrary parameters. (c) Example of an open hysteresis cycle in the magnetization field chart. The shadowed region is the area of the cycle and the coercive field is indicated in blue. (d) Schematic of the experimental system; 40 μL of a suspension of MNPs at a concentration such that dipolar interactions are negligible.

logarithm sense) is not located in the linear regime, but rather far from it. As a drawback, these "non-linear benefits" (multi-channel fitting and higher sensitivity) demand paying a price in the computational cost, as closed relationships are simply not analytically derivable. For this task, solving Langevin dynamics for MNPs, which even allows for including dipolar and hydrodynamic interactions in dense suspensions,[42,43] is simply too expensive to tackle the whole range of parameter space. In the context of parameter extraction, however, the controllable dilute regime is of primary interest and solving the (non-linear) Fokker–Planck equation (FPE) for the time-dependent MNP orientational distribution has been the common route,[41,44–47] although other approximate alternatives exist.[48] By expanding the sought distribution in an orthogonal functional basis, the FPE leads to an infinite hierarchy of ordinary differential equations (ODEs), which is truncated to achieve the desired precision.[46] "Non-linear sensing" has been recently used by Yoshida *et al.*[24] in a method which fits the experimental values of the magnetization harmonics series to simultaneously determine the distribution of the magnetic moment of MNPs, relaxation times and the particle concentration of even bimodal distributions. The proposed iterative method[24] requires an accurate numerical solution of the FPE over each iteration and a rather complex algorithm to do it efficiently.

Phenomenological relationships circumvent the need for costly FPE numerical solvers and substantially reduce the fitting effort. They are applied to determine experimentally accessible quantities and have proven to be highly effective in measuring solution viscosities,[49] fluid temperature,[50,51] simultaneous viscosity and temperature,[52] and even temperature and particle size.[53] However, their validity is typically limited to specific parameter ranges and require prior calibration with a well-known system before they can be used to determine other quantities. This limitation certainly constrains their predictive capacity.

In this work, we propose an optimal combination of both approaches. First, we numerically solved the FPE over the whole range of governing parameters, and then we integrated all this information into an analytical phenomenological relationship for the AC magnetic hysteresis area which is universal in the sense it is valid for any combination of external parameters (frequency f and field intensity H_0). Instead of fitting a broad range of magnetic parameters, such as the amplitude and phase of multiple harmonics,[21] a key point to achieve our goal in efficiency is to restrict our analysis to the AC magnetic hysteresis area, which is the only fitted parameter used to extract system's properties from a series of signals at varying f and H_0 values. The protocol for parameter estimation is based on an efficient combination of parallel-tempering Monte Carlo followed by second-order accurate Gauss–Newton methods. We first validated its accuracy and precision using signals from accurate Langevin dynamics simulations. Then we applied it to experiments with uncoated MNPs, measuring their size and magnetization as well as the viscosity of several embedding solvents (glycerol–water mixtures). In more stringent biosensing tests, we determined nanometer variations in size of MNPs coated with dextran, then conjugated with proteins and finally after biomolecular recognition with target biomolecules. Our estimates for particle size distributions are compared with NTA and DLS and with the much more "exact" transmission electron microscopy (TEM); the magnetization of particles was compared with a superconducting quantum interference device (SQUID) and we estimated solvent viscosities with an outstanding agreement with standard rheometers. The results are in perfect agreement with TEM and SQUID and improve the precision and accuracy of NTA and DLS size estimation. As a relevant conclusion, we highlight that the present theoretical–experimental integrated approach upgrades AC-magnetometry as a stand-alone experimental device able to determine a significant list of properties of both solvents and particles, being of particular relevance for biosensing.

Universal relationship for the magnetic hysteresis area

We consider a number $\mathcal{N}$ of suspended magnetic nanoparticles (MNPs) in a volume $\mathcal{V}$ (concentration $c = \mathcal{N}/\mathcal{V}$). The magnetic moment of each MNP is m_0 and the saturation magnetization $M_s = m_0/[(4/3)\pi r_c^3]$ is determined by their magnetic core radius r_c. In general, MNPs may present a coating layer of thickness δ, such that their hydrodynamic radius is $r_h = r_c + \delta$. The solution was exposed to an AC magnetic field $H(t)$ oscillating in the z direction at an angular frequency of $\omega = 2\pi f$. The delay in the system's magnetization $M(t)$ with respect to $H(t)$ leads to some heat dissipated per cycle, equal to the area $\mathcal{A}$ enclosed in the H–M chart (Fig. 1c). In deriving a general relationship for this magnetic hysteresis area, it is convenient to reduce the number of free parameters by working with non-dimensional variables. The non-dimensional area, defined as $\tilde{\mathcal{A}} \equiv \mathcal{A}/(\mathcal{N}\mu_0 H_0 m_0)$, only depends on the dimensionless frequency $\tilde{\omega} = \omega\tau_B$ and the field amplitude $h_0 = \mu_0 m_0 H_0/k_B T$. Here μ_0 is the magnetic permeability of vacuum and we recall the Brownian rotational relaxation time $\tau_B = 4\pi\eta r_h^3/(k_B T)$. To extract the general relationship $\tilde{\mathcal{A}} = \tilde{\mathcal{A}}(\tilde{\omega}, h_0)$, we have solved the Fokker–Planck equation for the time-dependent probability distribution of the magnetization of a single particle (see the Materials and methods section). This approach is valid for dilute suspensions of MNPs that relax predominantly *via* the Brownian mechanism, as in such a case the total magnetization is simply proportional to the single-particle magnetization and the phenomena related to Néel relaxation, including anisotropy barrier crossings, are negligible. The limit of validity of the dilute regime can be estimated from the strength of particle–particle interactions‡ leading to $c < 10^{16}$ MNPs per mL (or $c < 15$ μM). We note that these are not

‡Magnetic (dipole–dipole) interactions between MNPs become relevant once their magnetic energy (taking its maximum in an aligned configuration) $U_{mag} = (\mu_0 m_0^2)/(2\pi r^3)$ overpowers the thermal energy $k_B T$. At ambient temperature, the condition $U_{mag} < k_B T$ implies particle–particle distances larger than, $r > [\mu_0 m_0^2/(2\pi k_B T)]^{1/3}$, ~60 nm. In terms of concentration $c \approx (1/r)^3$, this means that magnetic interactions are negligible for $c < 10^{16}$ MNP per mL which is of the same order as for aggregation.

actually "extremely dilute" concentrations by experimental standards: experiments presented hereafter were conducted for $c \approx 5 \times 10^{13}$ MNPs per mL, thus well within the dilute limit.

On the other hand, it is well known that the dominant relaxation mechanism depends on the applied magnetic field. Specifically, when the amplitude of the AMF is sufficiently high for the magnetic moment of the particles to overcome the anisotropy barrier, the Néel mechanism may become dominant. This imposes an upper limit on the values of h_0 for which the phenomenological equation remains valid. This limit is determined by the condition $U_{ext} > U_{anis}$, where the energy of the particles under an external field is given by $U_{ext} = \mu_0 H_0 M_s V_c$, and the energy required to cross the anisotropy barrier is $U_{anis} = KV_c$. This leads to an inequality $H_0 < K/(\mu_0 M_s)$. For cobalt ferrite nanoparticles, which typically have an anisotropy constant of $K \approx 10^5$ J m^{-3} and a saturation magnetization of $M_s = 2 \times 10^5$ A m^{-1}, this results in a maximum magnetic field amplitude of approximately 400 kA m^{-1}. This value is significantly higher than the magnetic fields used in this study and those achievable in most experimental setups.

We performed an extensive set of calculations using the FPE equation to calculate $\tilde{A}$ over a wide range of values of $\tilde{\omega}$ and h_0. The analysis of this extensive information leads us to derive an accurate empirical relationship for $\tilde{A}(\tilde{\omega}, h_0)$. This useful "universal" magnetic area empirical relationship is one of the important results of this work,

$$\tilde{A}_{emp}(\tilde{\omega}, h_0) = \frac{\tilde{\omega}/\tilde{\omega}_{max}}{[c_2 + c_1(\tilde{\omega}/\tilde{\omega}_{max})^{p_2}]^{p_1} \cdot [c_3 + (1+c_4)(\tilde{\omega}/\tilde{\omega}_{max})^{p_3}]^{p_4}} \quad (1)$$

with

$$\tilde{\omega}_{max} = 1 + 0.287 \frac{{h_0}^{0.891}}{1 + 5.52 {h_0}^{-1.16}} \quad (2)$$

and

$$p_0 = 1 - 0.45 \exp[-8.5 {h_0}^{-1.75}] \quad (3)$$

$$p_1 = \log\left(\frac{\pi h_0}{3\tilde{\omega}_{max}}\right) \cdot \left[\log\left(\frac{p_0+1}{p_0}\right)\right]^{-1} \quad (4)$$

$$p_2 = \frac{p_0 + 1}{p_1} \quad (5)$$

$$p_3 = 1.8 \quad (6)$$

$$p_4 = \frac{1 - p_0}{p_3} \quad (7)$$

Note that $\tilde{\omega}_{max}$ in eqn (2) corresponds to the frequency maximizing the area for a fixed intensity h_0. In other words, $\tilde{A}_{max}(h_0) = \tilde{A}_{emp}(\tilde{\omega}_{max}, h_0)$ is the maximum area obtained at h_0, given by:

$$\tilde{A}_{max}(h_0) = (1 - W)\frac{\pi h_0}{6} + 4W(1 - \ln[F(h_0)]) \quad (8)$$

where $W = \exp[-0.5 {h_0}^{-1.8}]$ acts as a weighting function that governs the transition between the linear ($W \approx 0$) and non-linear ($W \approx 1$) regimes and

$$F(h_0) = 1 + 0.3 {h_0}^{0.9} + 0.056 {h_0}^{1.65} + 1.54 \times 10^{-5} {h_0}^{3.21}.$$

We shall soon show that this maximum in the area (*i.e.*, in dissipated heat) takes place at the transition from the linear response (Debye model) to the non-linear regime. The coefficients c_i in eqn (1) are finally given by:

$$c_1 = \frac{p_0}{p_1 \cdot p_2} \cdot \tilde{A}_{max} - \frac{1}{p_1} \quad (9)$$

$$c_2 = \frac{c_1}{p_0} \quad (10)$$

$$c_3 = \left(\frac{1}{\alpha(h_0)\tilde{\omega}_{max} {c_2}^{p_1}}\right)^{\frac{1}{p_4}} \quad (11)$$

$$c_4 = \frac{1600}{{h_0}^{0.5}} \exp\left[-\left(6.33\tilde{\omega}^{0.18} + \frac{11}{h_0}\right)\right], \quad (12)$$

with

$$\alpha(h_0) = \frac{\pi h_0}{3(1 + 0.16 {h_0}^{2.05})^{\frac{1}{2.05}}}. \quad (13)$$

To illustrate the accuracy of eqn (1), Fig. 2a compares the area obtained from the solution of the FPE $\tilde{A}$ with $\tilde{A}_{emp}$ for $h_0 = 1$, 10, 100, and 1000 and a broad range of $\tilde{\omega}$ values. Differences between $\tilde{A}$ (symbols) and $\tilde{A}_{emp}$ (lines) are not observable with the naked eye. For more precision in the deviation, panel (b) presents a contour plot of the relative error between the FPE and eqn (1) spanning five orders of magnitude in both $\tilde{\omega}$ and h_0 ($0.01 \leq h_0 \leq 1000$). Remarkably, the relative error remains always below 1.5%. We provided a first test for this "universal area relationship" against experiments in Fig. 2c and d where we compared eqn (1) with values of the AC magnetic hysteresis area created using cobalt ferrite MNPs (dominated by Brownian relaxation). Measurements were conducted for frequencies in the range of 10–100 kHz and using several solvents, whose viscosities were modified by adding glycerol in water up to a volumetric percentage of 45%. This experimental test also illustrates the utility of deploying non-dimensional variables to gather results from quite different parameters in single master curves. Values of these non-dimensional parameters ($\tilde{\omega}$, h_0 and $\tilde{A}$) were obtained by taking the liquid mixture viscosity from ref. 54 (Table 3) and the hydrodynamic radius of MNPs provided by TEM (this approximation is valid since the particles are quasi-spherical and lack any surface coating). The experimental measurements in Fig. 2c and d show an excellent agreement with $\tilde{A}_{emp}$ in eqn (1), confirming it usability for parameter estimation in experiments.

Asymptotic regimes

We now analyze the different magnetization regimes and the different scaling laws for the magnetic area. Fig. 3a presents the contour plot of $\tilde{A} = \tilde{A}(\tilde{\omega}, h_0)$ from the numerical solution of the FPE. The plot reveals different regimes with distinct

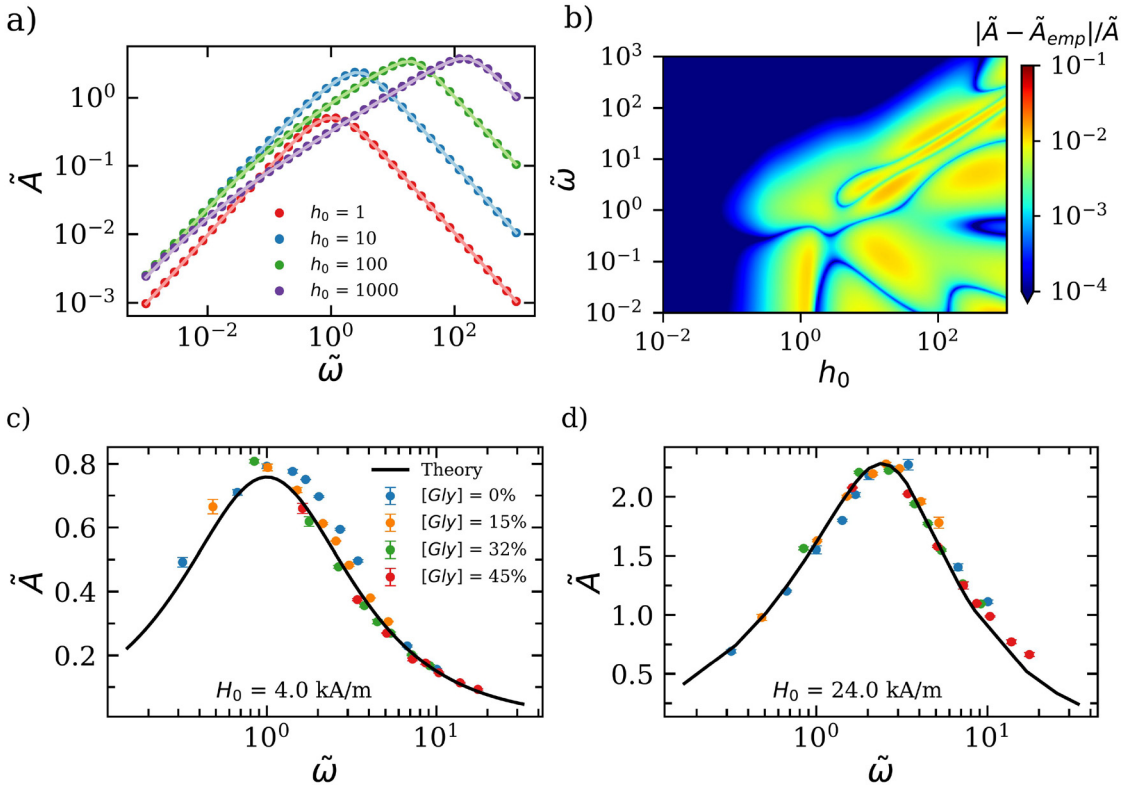

Fig. 2 (a) Comparison between the dimensionless magnetic area evaluated from the numerical solution of the Fokker–Planck equation (FPE) (dots) and the outcome of the empirical relationship in eqn (1) (lines) as a function of $\tilde{\omega}$ for different values of h_0. (b) Contour plot of the relative area difference between the FPE and eqn (1). (c and d) Comparison between the experimental values of the area as a function of the dimensionless frequency $\tilde{\omega}$ and the predictions of eqn (1) measured for field frequencies ranging from 10 kHz to 100 kHz and various glycerol concentrations, which alter the viscosity of the solution, for two field intensities: (c) 4 kA m^{-1} and (d) 24 kA m^{-1}. For the calculations, particles were modeled with a log–normal size distribution with a mean radius of $r_c = r_h = 13.6$ nm, a standard deviation of $\sigma_c = 1.3$ nm, and a saturation magnetization of $M_s = 179$ kA m^{-1}.

area scaling separated by a central region in the $(\tilde{\omega}, h_0)$ chart, where $\tilde{A}$ is maximum (see also Fig. 2a, c and d).

We start by stating that relationship 1 correctly recovers the linear response theory (LRT) result:

$$\tilde{A}_{\mathrm{LRT}}(\tilde{\omega}, h_0) = \frac{\pi h_0 \tilde{\omega}}{3(1+\tilde{\omega}^2)}. \tag{14}$$

The validity of the LRT or Debye model result (small h_0 or large $\tilde{\omega}$) is clearly deduced from Fig. 3b, showing the relative error of the LRT $|\tilde{A} - \tilde{A}_{\mathrm{LRT}}|/\tilde{A}$ (see also Fig. 3d). In terms of non-dimensional quantities, the validity domain of the LRT turns out to be extremely simple: $h_0 \lesssim 0.4$ for any $\tilde{\omega}$ and the region $h_0/\tilde{\omega} < 1$. From the definitions given above, one realizes that the $h_0/\tilde{\omega}$ group represents the ratio between the energy provided by the external field to the magnet and the energy dissipated by the viscous torque. Hence, the LRT works when the viscous energy dissipation is faster than the external power reaching the magnet. In passing, the color scales of Fig. 3a and c indicate that the nondimensional area is bounded such that $\tilde{A} < 4$. Indeed, it is constrained by the rectangle defined by the x-bounds $|h(t)/h_0| < 1$ and the y-bounds $|\tilde{M}(t)| \leq 1$, where $\tilde{M}(t) \equiv M(t)/(\mathcal{N} m_0)$ and $h(t) \equiv \mu_0 m_0 H(t)/k_B T$. Note that such a constraint in the non-dimensional area is clearly not satisfied by the linear approximation in eqn (14).

We now consider the different asymptotic regimes observed as one varies the field intensity h_0. At low field amplitudes ($h_0 < 1$), the thermal energy surpasses the magnetic energy, leading to a predominantly randomized orientation of the magnetic moments. As a result, the system exhibits negligible average magnetization and an almost imperceptible hysteresis loop area. This region (small h_0) roughly corresponds to the regime where LRT is valid, predicting a linear increase in $\tilde{A}$ with h_0 (as shown in eqn (14)). As h_0 increases (with $\tilde{\omega}$ held constant), the area $\tilde{A}$ reaches a peak before decreasing again at higher field amplitudes. This behaviour represents a genuine non-linear effect, not captured by the LRT (see Fig. 4a illustrating the H–M chart and the ESI† for more details). On further increasing h_0, the magnetic moments tend to remain aligned with the field direction for most of the cycles, entering the saturation regime. Only when the applied field approaches the coercitivity value H_c (Fig. 1c) do the moments quickly reorient. Consequently, the hysteresis loop shrinks as h_0 increases further, as shown in Fig. 4a and c. In this high intensity h_0 regime, the area scales as:

$$\tilde{A}(\tilde{\omega}, h_0 \gg 1) \approx 8\tilde{\omega}^{0.55} h_0^{-0.45} \tag{15}$$

Concerning the frequency response (Fig. 4b and d), the AC magnetic hysteresis area is small at low frequencies

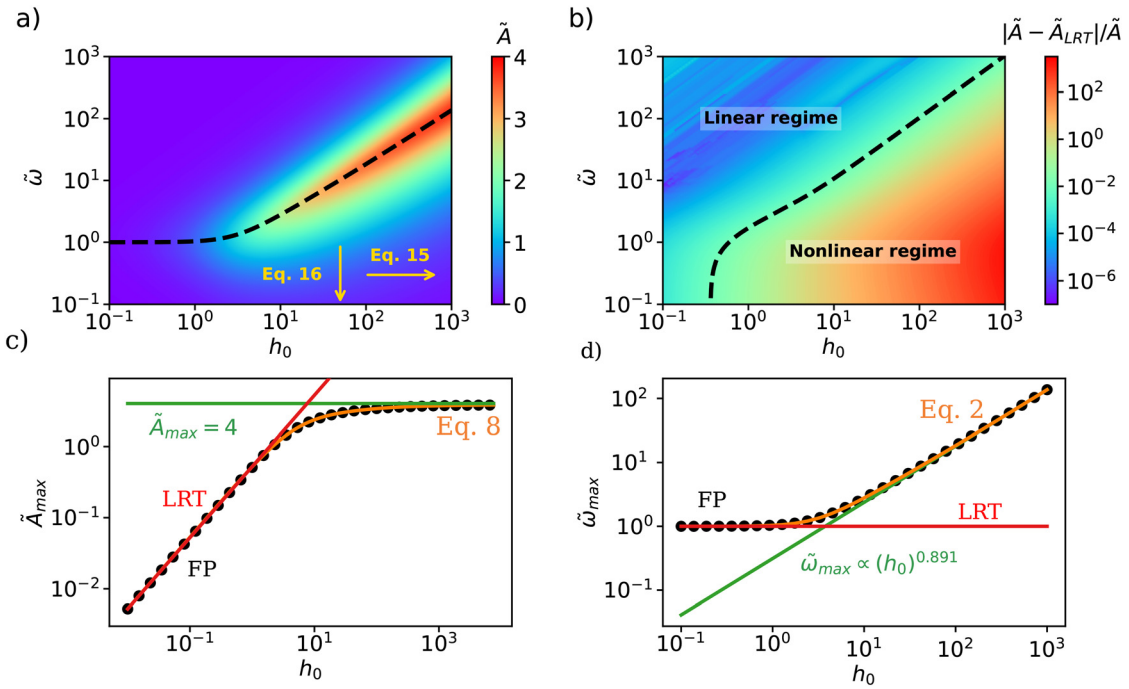

Fig. 3 (a) Two-dimensional colormap depicting the variation of $\tilde{A}$ as a function of the dimensionless parameters $\tilde{\omega}$ and h_0 obtained by numerically solving the FPE. The black dashed line represents the value of $\tilde{\omega}$ that maximizes the area for each h_0. (b) Two-dimensional colormap illustrating the relative error between the area predicted by LRT and the area obtained from the FPE as a function of the dimensionless parameters. The black dashed line highlights the isocontour where the relative error reaches 1%. (c) Maximum cycle area as a function of h_0. The green line represents the theoretical upper bound, the red line corresponds to the LRT prediction, and the orange line depicts the prediction from eqn (8). (d) Value of $\tilde{\omega}$ that maximizes the area as a function of h_0. The red line shows the LRT prediction, the green line represents the asymptotic scaling $\tilde{\omega}_{max} \propto {h_0}^{0.891}$, and the orange line corresponds to eqn (2).

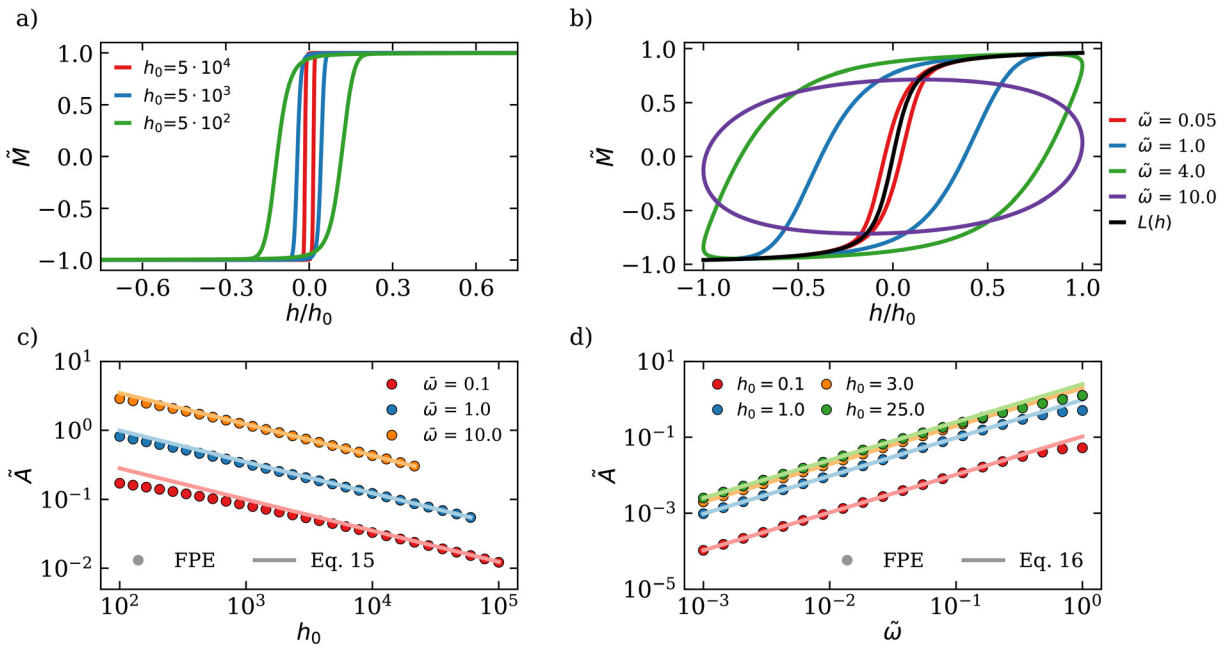

Fig. 4 (a and b) Hysteresis loops plotted in terms of the scaled field $h(t)/h_0$ and the dimensionless magnetization $\tilde{M}$. In panel (a), $\tilde{\omega} = 1$ and h_0 varies with high values. In panel (b), h_0 = 25 is fixed and the loops are computed for various values of $\tilde{\omega}$. The static response described by the Langevin equation $L(h)$ is shown as a black line. (c) Variation of the AC magnetic hysteresis area with h_0 for large values and different values of $\tilde{\omega}$. (d) AC magnetic hysteresis area as a function of $\tilde{\omega}$ in the low-frequency regime ($\tilde{\omega} \ll 1$) for various values of h_0. In panels (c) and (d), the dots indicate the results obtained by solving the FPE and the lines indicate the predictions of eqn (15) and (16), respectively.

($\tilde{\omega} < 1$) because the magnetization efficiently responds to the time variation of the applied field; in the limit $\tilde{\omega} \to 0$, the hysteresis vanishes and the system magnetization M follows the static behavior described by the Langevin function (Fig. 4b, black line). High intensity $h_0 > 1$ and low frequency ($\tilde{\omega} < 1$) are well outside the LRT. Fig. 4d shows the scaling law for the area in this region, which follows as:

$$\tilde{\mathcal{A}}(\tilde{\omega} \ll 1, h_0) = \alpha(h_0)\tilde{\omega}, \tag{16}$$

where $\alpha(h_0)$ is given in eqn (13) and for small h_0, it converges to $\alpha_{\mathrm{LRT}}(h_0) = \pi h_0/3$. Finally, in the high-frequency regime, $\tilde{\omega} \gg 1$, the external field oscillates faster than the magnetic relaxation time, τ_{B}, and the magnetic moments can no longer follow the rapidly changing field. This leads to a smaller magnetization and a reduced AC magnetic hysteresis area. At low field values $h_0 < 1$ the maximum area takes place for $\tilde{\omega}_{\max} = 1$. This result is consistent with a sort of stochastic resonance correctly captured by LRT (eqn (14)), which predicts more dissipation when the relaxation rate $1/\tau_{\mathrm{B}}$ coincides with ω. However, the non-linear response to high external fields alters the location of the maximum dissipation towards larger frequencies $\tilde{\omega}_{\max} > 1$, as shown in Fig. 3a and d (black dashed line). The LRT also severely fails in this regime as its maximum area increases without bounds with h_0, as $\tilde{\mathcal{A}}_{\mathrm{LRT,max}} = \pi h_0/6$. However, as previously noted (Fig. 4b and 3c), the maximum value of the non-dimensional area is capped at $\tilde{\mathcal{A}}_{\max} = 4$ and this limit is reached for $h_0 \to \infty$ following a logarithmic trend. The agreement between $\tilde{\mathcal{A}}_{\max}$ in eqn (8) and the FPE's maximum area is perfect, as shown in Fig. 3c.

Simultaneous determination of system's properties by cost-error minimization

The excellent accuracy of the universal empirical relationship for the magnetic hysteresis area (eqn (1)) opens a route to a fast determination of the multiple systems' properties controlling the area. The experimental setup imposes the magnetic field amplitude H_0 and frequency f that, in non-dimensional form, are noted as $\xi = \{h_0, \tilde{\omega}\}$. The collection of unknown "fundamental system's variables" is notated as $\boldsymbol{\lambda} = \{r_{\mathrm{h}}, m_0, \eta, T, \mathcal{N}\}$ and contains the hydrodynamic radius and magnetic moment of MNPs, the solvent viscosity, and the temperature and number of MNPs. Yet, in many practical applications, these properties, $\boldsymbol{\lambda} = \{r_h, m_0, \eta, T, \mathcal{N}\}$, are not single-valued but rather follow a distribution. We will characterize the first two moments of such distributions $p_i(\lambda_i)$: the mean $\langle\lambda_i\rangle$ and the variance $\sigma_{\lambda_i}{}^2$. The shape of these marginal distributions $p_i(\lambda_i)$ such that $p(\boldsymbol{\lambda}) = \Pi_i p_i(\lambda_i)$ are part of the model: typically we used a delta for single-valued variables, a Gaussian or a log–normal distribution depending on the specific variable (see the Materials and methods section). This leads to a generalization of the vector of unknown variables, which is noted as $\boldsymbol{\Lambda} = \{\langle\boldsymbol{\lambda}\rangle, \boldsymbol{\sigma}_{\boldsymbol{\lambda}}\}$. The "theoretical" average area in dimensional units was obtained from relationship 1 weighted by $p(\boldsymbol{\lambda}; \boldsymbol{\Lambda})$ as:

$$\mathcal{A}_{\mathrm{the}}(\boldsymbol{\Lambda}, \xi) = \mathcal{N}\mu_0 H_0 \int \tilde{\mathcal{A}}_{\mathrm{emp}}(\tilde{\omega}(\boldsymbol{\lambda}, f), h_0(\boldsymbol{\lambda}, H_0)) \cdot m_0 \cdot p(\boldsymbol{\lambda}; \boldsymbol{\Lambda}) \mathrm{d}\boldsymbol{\lambda} \tag{17}$$

where we recall that h_0 depends on the vector of parameters $\boldsymbol{\lambda}$ *via* m_0 and T. Our target is to evaluate the value $\boldsymbol{\Lambda} = \boldsymbol{\Lambda}^*$ that minimizes the difference between the experimental area $A_{\mathrm{exp}}(\boldsymbol{\Lambda}^*)$ and the "theoretical" expression given by eqn (17). To this end, we have developed a "parameter estimator" that finds $\boldsymbol{\Lambda}^*$, minimizing a cost-error function ($\mathcal{C}_{\min} = \mathcal{C}(\boldsymbol{\Lambda}^*)$) given by:

$$\mathcal{C}(\boldsymbol{\Lambda}) = \sum_{i=1}^{N_{\mathrm{ex}}} \frac{\left|\mathcal{A}_{\mathrm{the}}(\boldsymbol{\Lambda}, \xi^{(i)}) - \mathcal{A}_{\mathrm{exp}}(\xi^{(i)})\right|}{\mathcal{A}_{\mathrm{exp}}(\xi^{(i)})} \tag{18}$$

Importantly, the sum in eqn (18) runs over a number of independent experimental measurements N_{ex} (typically between 8 and 24) under varying frequencies and field-intensities: $\xi^{(i)}$ with $i \in [1, N_{\mathrm{ex}}]$. The searching protocol combines an initial stochastic search in the parameter space (parallel tempering Monte Carlo), followed by an accurate deterministic minimization (second-order Gauss–Newton scheme). Both steps are detailed in the Materials and methods section. The parallel tempering Monte Carlo (MC)[55] is able to locate the minima under quite general starting conditions in the parameter space. Once the cost function levels below the chosen threshold, the scheme uses the second order Gauss–Newton (GN) algorithm to refine the solution. The resulting fitting protocol is quite fast and we made it available in the repository.[56] It is implemented in C++, with Python bindings for easy usage.

To validate the protocol, we now assess its precision by comparing with numerical simulations with exactly known system parameters. In the next section, we used the parameter estimator to determine experimental data related to MNPs and the solution viscosity.

Assessing the accuracy in the parameter estimation from numerical simulations

In order to validate the fitting methodology and estimate its accuracy, we performed Brownian dynamics (BD) simulations[22] of MNPs under an AC field. The magnetic radius r_{c} and coating thickness δ used in the BD runs were chosen to closely match the experimental values (see below). Additionally, consistent with the typical distribution of nanoparticle sizes,[57] we sampled r_{c} values from a log–normal distribution with a mean $r_{\mathrm{c}} = 15$ nm and varying polydispersities (standard deviations $\sigma_c/r_c \in [0.1, 0.5]$). We explored several coating thicknesses $\delta \in [0, 12.5]$ nm and a saturation magnetization of $M_{\mathrm{s}} = 150$ kA m^{-1}. In this test, A_{exp} corresponds to the results from BD simulations. As noted above, the cost function is based on a set of N_{ex} experiments consisting of frequency dependence studies of the AC magnetization cycles (see the Materials and methods section) at different field intensities (4, 12 and 24 kA m^{-1}), leading to a total of $N_{\mathrm{ex}} = 24$ cases, which are fitted simultaneously. This set of conditions mirrors those used in the experiments.

It is important to note that the accuracy of the $\mathbf{\Lambda}^*$ prediction tends to decrease as the number of experiments used in the fits is reduced. As shown in the ESI,† achieving a reliable estimation of the parameters requires the utilization at least two different field intensities and 4–5 frequency values.

To optimize any fitting procedure, it is important to restrict the unknown parameters. However, as a first stringent test, we set $\delta = 0$ (*i.e.*, no coating, so the hydrodynamic and magnetic radii coincide, $r_h = r_c$) and assumed that M_s is the same in all the particles, so $m_0 = (4/3)\pi M_s r_c^3$. Under these assumptions, we simultaneously estimated the average core radius $\langle r_c \rangle$, the standard deviation of distribution σ_c, the number of particles in the suspension, and the saturation magnetization M_s for different values of σ_c.

Table 1 Parameters of MNPs determined by applying the present method to BD simulations, in which M_s = 150 kA m^{-1}, r_c = 15 nm, $\mathcal{N} = 1 \times 10^5$, and σ_c takes various values that are indicated in the first column

Simulations	Present method			
σ_c/r_c	σ_c/r_c	r_c (nm)	M_s (kA m^{-1})	$\mathcal{N}$
0.1	0.099 ± 0.006	15.0 ± 0.1	150.5 ± 0.6	(0.998 ± 0.005) × 10^5
0.25	0.241 ± 0.008	15.2 ± 0.2	150.3 ± 0.2	(0.992 ± 0.002) × 10^5
0.5	0.500 ± 0.005	14.9 ± 0.1	149.3 ± 0.2	(1.000 ± 0.001) × 10^5

The results summarized in Table 1 indicate that the estimated values for M_s, r_c, σ_c, and $\mathcal{N}$ closely match the "true" values used in the BD simulations. In all instances, the relative error remains consistently of the order of 1% or smaller for each parameter, highlighting the method's high accuracy in determining unknown system parameters.

In a second test, we evaluated the ability of the parameter estimator to quantify variations in hydrodynamic size when a coating is added to the particles. Following the experimental approach, we assumed that the bare MNPs had already been characterized, with r_c, M_s, and σ_c known as fixed parameters. Thus, the goal was to determine the hydrodynamic radius of the particles ($r_h = r_c + \delta$) by sampling over δ. We studied five different cases with increasing values of δ. The results, shown in Fig. 5a, demonstrate that this method can accurately determine the hydrodynamic size of the particles. In particular, an analysis of the relative error between the fitted hydrodynamic radius and the value used in the simulations (Fig. 5b) reveals that the error is consistently below 0.15%. Fig. 5c and d present the dependence of the relative error in the estimated system's parameters with the number of area measurements N_{ex}. Notably, about N_{ex} = 10 area measurements (at different fields and frequencies) are enough to obtain relative errors of about 10^{-2} in the magnetic saturation M_{sat} and the average particle radius r_c. The dispersion in size distribution σ_c requires about 20 measurements to yield such one

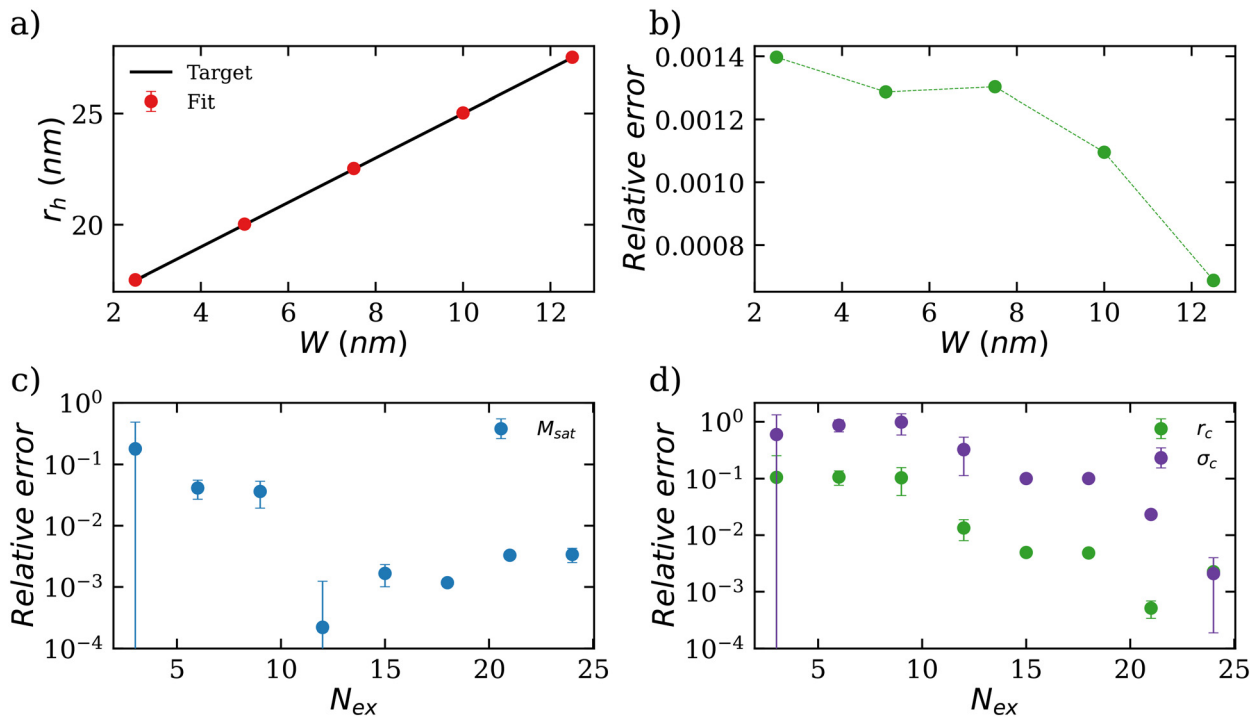

Fig. 5 (a) Hydrodynamic radii of the MNPs for various coating widths determined using the fitting algorithm (red dots) compared with the values used in the simulations (black line). (b) Relative error between the expected hydrodynamic radius and the values obtained from the fitting. (c and d) Relative error between the estimated parameters and the values used in the BD simulations (M_s = 150 kA m^{-1}, r_c = 15 nm, and $\sigma_c = 0.1 r_c$) as a function of N_{ex}. Panel (c) shows the results for M_s, while panel (d) presents the results for r_c (green) and σ_c (purple), corresponding to the average particle size and the standard deviation, respectively. The results correspond to the datasets with three field intensities: H_0 = 4, 12, and 24 kA m^{-1} and varying numbers of field frequencies (see the additional data in the ESI†).

percent error. Notably, the errors decrease down to the 0.1% range for N_{ex} ~25, which is the suggested value.

Determining system's properties from experiments

Next, we applied the same methodology to determine multiple experimental parameters in different situations. In all experiments, we used cobalt ferrite nanoflowers. First, we employed uncoated ("plain") p-MNPs with –COOH groups on their surface to provide colloidal stability. From the measurements of the cycle areas, we determined their saturation magnetization, the distribution of crystal sizes and the concentration of particles.

Once these particles have been characterized, we used them to determine the viscosity of glycerol solutions at different concentrations. Finally, we used the same method to study how the hydrodynamic size of the particles changes when a dextran coating is added and they are functionalized with ligands that interact with other biomolecules in the solution.

Determination of the core radius and magnetic moment of p-MNPs

To demonstrate the potential of the method for determining the crystal size and magnetic moment of MNPs, we analyzed raw experimental data on the AC magnetic hysteresis area of p-MNPs. Using our parameter estimator, we determined the core size and magnetic moment of bare MNPs. To validate these predictions, we compared them with TEM, NTA, and DLS measurements for particle size and SQUID measurements for magnetic moment. The experimental results of the area against the frequency are shown in Fig. 6a, in which the circles indicate experimental values and the lines indicate eqn (1) using the best parameter estimation (obviously $\delta = 0$ was fixed). The comparison between the values of our parameter estimator and the experimental ones can be found in Table 2.

There is a perfect agreement between the present method and the sizes determined from TEM images (ESI†), which is the most reliable and exact size-measurement device. DLS slightly overestimates the hydrodynamic size but the agreement is also very good. Finally, NTA presents a much larger inaccurate value because our particles are below the NTA limit

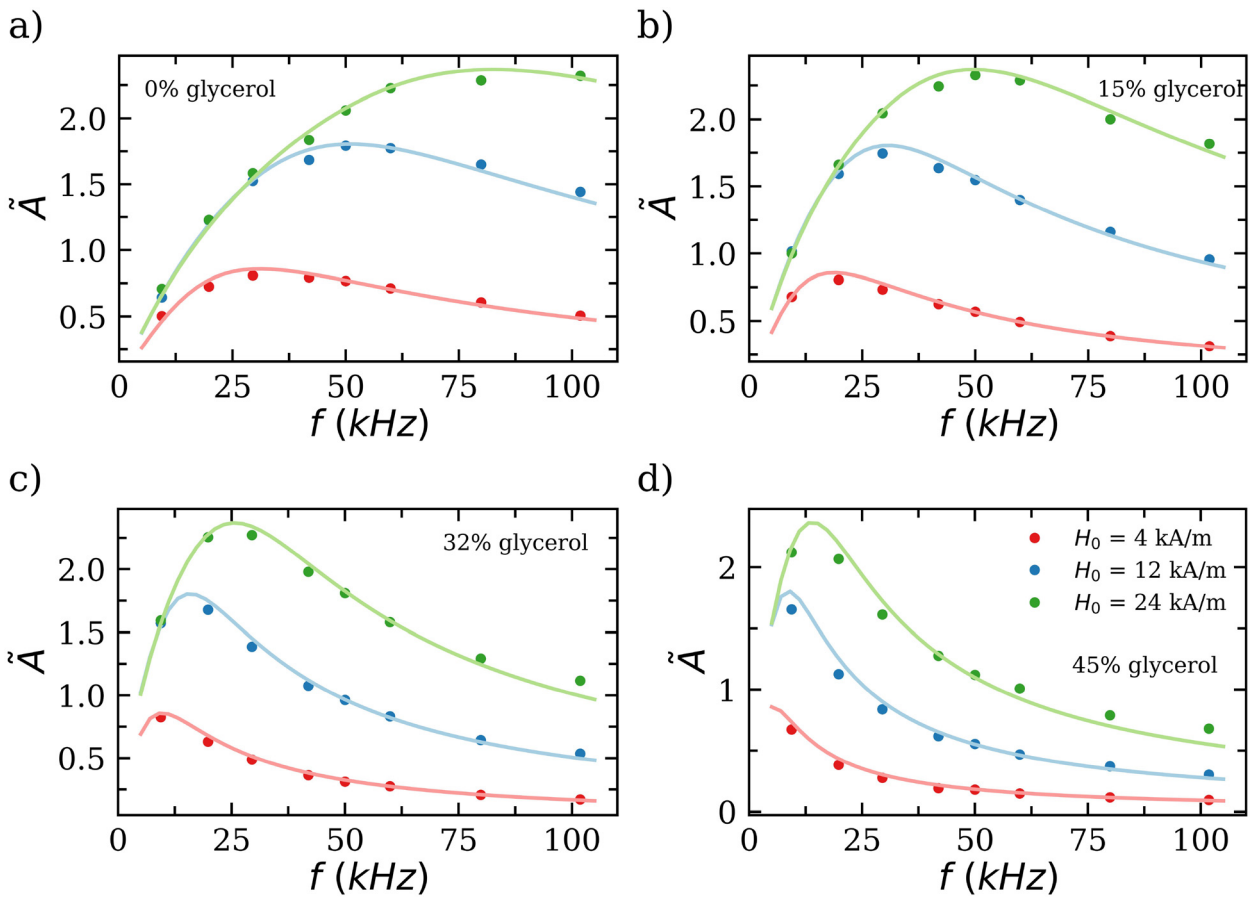

Fig. 6 AC magnetic hysteresis area as a function of field frequency for three different field amplitudes: 4 kA m^{-1} (red), 12 kA m^{-1} (blue), and 24 kA m^{-1} (green) measured for water–glycerol mixtures at various glycerol concentrations: (a) 0% by volume, (b) 15%, (c) 32%, and (d) 45%. The dots represent experimental data, while the solid lines correspond to the fits obtained using the presented algorithm.

Table 2 Mean hydrodynamic radius (r_h) obtained using the present method compared with the reported values through different methods in ref. 58

Present method	TEM	DLS	NTA
13.6 ± 0.2 nm	13.58 nm	15 nm	~20 nm

of detection (~20 nm) which significantly biases the measure towards the largest particles of the ensemble. TEM images (ESI†) also provide the standard deviation in size, σ_c = 1.6 nm, which agrees with our estimation σ_c = (2.4 ± 0.2) nm extracted by assuming a log–normal distribution for r_c into the fitting protocol (see the Materials and methods section). The size standard deviation is slightly overestimated by our method, which might be a consequence of the dispersion in M_s amongst the particles due to variations in the relative orientation of the different coalescent cores forming these particles. In any case, the fitted value of the effective saturation magnetization is M_s = 166.5 ± 0.2 kA m^{-1}, which is also in close agreement with the value obtained using SQUID measurements, M_s = 179 kA m^{-1}. The estimated number of particles in the suspension was 2.12 × 10^{12}, which for the volume employed in the experiments 40 μL corresponds to a concentration of 5.3 × 10^{13} MNP per ml (or ~80 nm). This value is in agreement with the concentration of ~3 × 10^{13} MNP per ml estimated from the experimental mass density 1 g_{Fe+Co} L^{-1} of roughly spherical particles with a radius of 13.6 nm and a density of ~5.25 g cm^{-3}. Possible differences between both estimations arise because particles are not perfect spheres but nanoflowers (ESI†), so their volume is smaller than the spherical estimation.

Determination of the viscosity of glycerol solutions at different concentrations

To demonstrate the capability of the fitting algorithm to determine the solution viscosity, we revisited the experimental data in Fig. 2c and d corresponding to a set of samples with varying viscosities obtained from mixtures of glycerol and water at different volume percentages (see the Materials and methods section). In this case, we left the viscosity as the only free parameter in the fitting scheme and self-consistently deployed the protocol as a viscosimeter. We performed measurements for glycerol solutions in water with glycerol of 0%, 15%, 32%, and 45% in volume. For each concentration, we measured the AC magnetization cycles at different field frequencies and at three field intensities (H_0 = 4, 12, and 24 kA m^{-1}). The viscosity is taken as the sole free parameter in the fits and, to use a self-consistent approach, the size of MNPs is first characterized by the fitting protocol in pure water (*i.e.*, 0% glycerol). The results are summarized in Table 3, along with the viscosities based on the empirical formula presented in ref. 54. We observed

Table 3 Comparison between the literature values of the viscosity of different mixtures of glycerol concentration and water at 25 °C and the measured value using the presented algorithm

Glycerol concentration (% volume)	Fitted viscosity (mPa s)	Literature viscosity (mPa s)
0	0.871	0.893
15	1.450	1.444
32	2.80	2.80
45	5.134	5.22

almost perfect agreement between our results and the expected values, confirming that this method is highly effective as a viscosimeter.

To further reinforce the protocol, in Fig. 6, we compared the experimental results of the area with the fits for all the measurements, showing that the values obtained through the fitting algorithm reproduce the experimental ones almost exactly.

Determination of the hydrodynamic radius of coated MNPs with different molecules on their surface

To highlight the potential of the method to analyze more complex scenarios, we applied our fitting algorithm to study variations in the hydrodynamic size of the particles when their surface is modified by changing the attached molecules. Specifically, the four types of surfaces studied are summarized in the insets of panels (a)–(d) in Fig. 7: panel (a) shows the previously studied p-MNPs; panel (b) depicts cobalt ferrite MNPs coated with dextran (D-MNPs); panel (c) represents MNPs bioconjugated with receptors (f-D-MNPs); and panel (d) illustrates f-D-MNPs after being immersed in a 2 μM solution and allowed to reach chemical equilibrium. The experimental values of the hysteresis areas under different field conditions (blue and red symbols in Fig. 7), as well as the mean hydrodynamic radius obtained through NTA measurements of the translational diffusion coefficient, are taken from ref. 22 and 58. The magnetic properties of the particles, such as M_s, r_c, and σ_c, may slightly differ from previously measured values due to batch-to-batch variations in synthesis. These differences can lead to slight changes in core size and the dextran coating may prevent surface oxidation, potentially altering the M_s value.[59] Situations where initial knowledge of certain parameters is partial or inaccurate are common; however, the flexibility of the MC scheme allows for easy adaptation. We employed a modified cost function with a soft bias toward the available initial information: $\mathcal{C}(\boldsymbol{\lambda}) = \mathcal{C}(\boldsymbol{\lambda}) - k_M \cdot (M_s - M_s^0)^2 - k_r \cdot (r_c - r_c^0)^2 - k_\sigma \cdot (\sigma_c - \sigma_c^0)^2$, where the parameters with superscript '0' correspond to values for p-MNPs, providing a reliable initial guess. This approach restricts the parameter search to the critical region defined by previously measured values. The hydrodynamic radius values obtained through this method are pre-

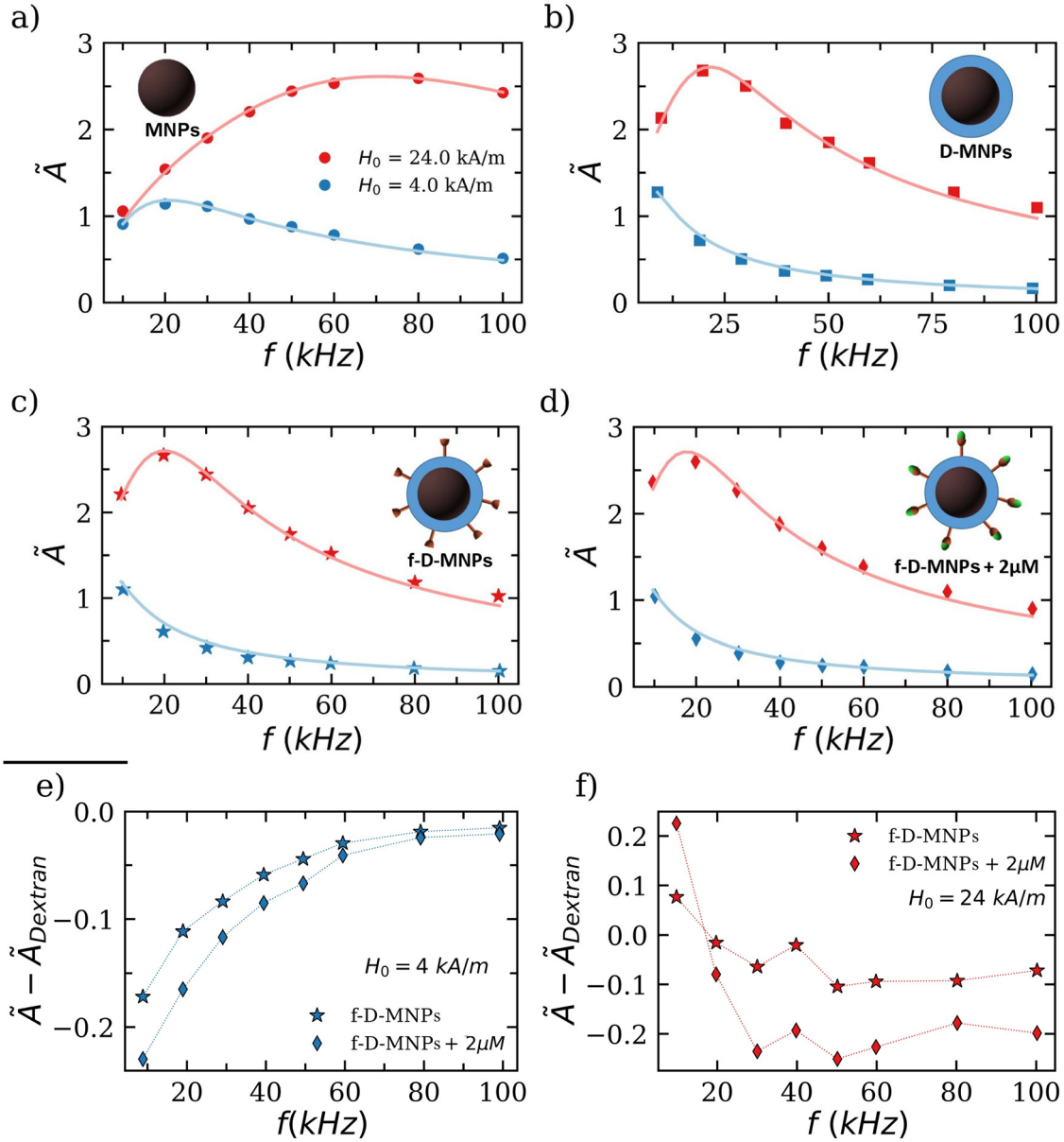

Fig. 7 (a–d) Experimental measurements (symbols) and fits using the present method for the average nondimensional magnetic area against the frequency. The cases correspond to (a) particles without coating (p-MNPs), (b) particles coated with dextran (D-MNPs), (c) particles coated with dextran and functionalized with a recognition receptor (f-D-MNP), and (d) f-D-MNPs in a 2 μM solution of the target protein. (e and f) Area difference $\Delta\tilde{\mathcal{A}}_{case} \equiv \tilde{\mathcal{A}}_{case} - \tilde{\mathcal{A}}_{D-MNP}$ for H_0 = 4 kA m^{-1} (e) and H_0 = 24 kA m^{-1} (f) by comparing the cases of f-D-MNPs (stars) and f-D-MNPs + 2 μM (diamonds).

sented in Table 4 (column 1) and compared with NTA measurements.

The results obtained through the fitting of the magnetic areas are quite close to the experimentally measured values. However, as mentioned in the introduction, NTA measurements are often difficult to reproduce due to their strong dependence on specific experimental conditions (*e.g.*, particle concentration[28] and device configuration[60,61]). Therefore, we do not expect perfect agreement between this method and NTA measurements. In this context, the precision and accuracy tests for the current AC magnetometry integrated approach, validated against controlled BD simulations (Table 1), suggest that the results shown in Table 4 for this method are more precise than those obtained with NTA measurements. In this

Table 4 Comparison between the hydrodynamic radius measured from NTA and the present method

Surface	r_h (NTA) [nm]	r_h (present method) [nm]
Dextran	23.1 ± 0.2	21.8 ± 0.4
f-Dextran	25.3 ± 0.3	22.5 ± 0.1
f-Dextran + 2 μM	26.2 ± 0.6	23.4 ± 0.1

line, it is interesting to observe in Fig. 7e and f the hysteresis area difference $\Delta\tilde{\mathcal{A}}_{\text{case}} \equiv \tilde{\mathcal{A}}_{\text{case}} - \tilde{\mathcal{A}}_{\text{D-MNP}}$ between the dextran-coated D-MNPs and the cases with functionalized particles (f-D-MNPs) and adsorbed proteins (f-D-MNPs + 2 μM). These differences are subtle and depend on a non-trivial way with the field intensity and the frequency. For instance, the difference (and thus the resolution) is quite poor $\Delta\tilde{\mathcal{A}}_{\text{case}}(h_0, \tilde{\omega}) \approx 0$ if one uses high frequencies and low intensities (linear regime, H_0 = 4 kA m^{-1}) or, also, when using low frequencies and high intensity (H_0 = 24 kA m^{-1}). This illustrates the importance of analyzing a broad range of frequencies and intensities to ensure consistent and accurate parameter estimations.

Conclusions

We have derived an analytical expression for the AC magnetic hysteresis area created by a dilute suspension of Brownian-type MNPs when exposed to alternating magnetic fields (AMFs) of arbitrary intensity and frequency. This "universal relationship" for the area agrees within 1% with the numerical solution of the non-linear Fokker–Planck equation for these particles, which present a blocked magnetic moment fluctuating due to Brownian rotation. Being a function of the non-dimensional groups governing this phenomenon (field amplitude and frequency), this analytical relationship opens up new ways to measure a list of relevant variables pertaining to both the particles and solvents. To this end, we developed a robust search algorithm to fit the experimental area from a series of signals at different frequencies and intensities. The fitting algorithm combines a Monte Carlo-based parallel tempering approach to locate the important region in the parameter space followed by a Gauss–Newton algorithm to accurately refine the measurements, notably up to ~1% agreement with the experimental data. The list of accessible quantities this hybrid theoretical–experimental methodology offers is surprisingly large, as it includes the particle's magnetic moment, average size, dispersion and concentration, and solvent properties such as viscosity and potentially temperature. This procedure is based on a relationship for the area which is valid under arbitrary conditions (provided particle concentrations smaller than $c \sim$ 10 μM) and for this reason, it does not require any prior calibration. Moreover, it does not require costly iterative solutions of the non-linear FPE to seek matching with a set of magnetic signals (magnetization harmonics). Instead, it is based on a quite sensitive unique signal (the hysteresis area) that allows for accurate analytical phenomenological mapping. These features provide an extremely fast characterization tool, which can be thus used in deep-science web-server applications, fed by experimental data from an oscillatory magnetometer.[62]

Concerning the overall time needed for the parameter estimations, including the experimental area measurement and the numerical fitting, we note that each area measurement takes about 1 minute. Hence, depending on the required error threshold (see Fig. 5c and d), the experimental part of the protocol typically takes between 10 and 25 minutes. Notably, once these data are introduced into the automated search, the parameter estimation only takes a couple of extra minutes (at most). These facts permit the qualification of the integrated protocol as "fast and accurate". For comparison, our experience indicates a time reduction in a factor of 3 with respective experiments using magnetic susceptibility meters and a substantial reduction in the automated search, as our scheme is based on an analytical relationship.

The accuracy and precision of the algorithm have been first measured against detailed Brownian dynamics simulations, showing ~1% relative differences with respect to the input values. The method was then tested against a series of experiments involving MNPs with increasing design complexity. Using plain MNPs, we found excellent agreement of ~1% with TEM measurements for the particle size and SQUID measurements for the magnetization and also with standard bulk rheometers for the solvent viscosity. In another series of tests, in the realm of biosensing applications, we used dextran-coated MNPs, which were then functionalized with protein receptors, and finally exposed to a solution with target biomolecules for molecular detection. The increase in particle size between these three steps were tiny (~2 nm) yet successfully detected by the new protocol, clearly surpassing the precision of standard experimental devices such as DLS and particularly NTA. This result proves the utility of this new tool in biomolecular sensing. Ongoing research will further explore another important benefit of this method, which is its ability to locally sense inhomogeneous systems within nanometer domains, accessing solvent properties (such as local viscosity in living cells[63]) or temperature-driven protein conformation variations. Measuring temperature at nanometer scales is also in the doable list. The solution of the nonlinear FPE can also be used to derive accurate empirical relationships for other relevant output quantities, such as magnetization harmonics, allowing for automated parameter extraction in magnetic particle imaging (MPI).[12–14] Also, here we focus on spherical particles, but the hysteresis area equation can be generalized to other shapes (rods, ellipsoids, *etc.*), introducing a tensorial form for the rotational diffusion of MNPs, with angular dependence along the principal magnetization axes. In conclusion, the present theory–experiment integrated approach enables, with a single experimental technique, the simultaneous characterization of multiple independent parameters of MNPs and solvents and opens new opportunities for transducing biomolecular recognition, conformational molecule changes or temperature reading in magnetic suspensions.

Materials and methods

Numerical solution of the Fokker–Planck equation

The numerical calculation of the hysteresis cycles was performed by solving the Fokker–Planck equation for $\Omega(t, \phi, \theta)$, which stands for the probability of one (isolated) MNP with the blocked magnetic moment pointing in a direction defined by the azimuthal angle ϕ and the polar angle θ at time t:

$$\frac{\partial \Omega(t,\phi,\theta)}{\partial t} = \nabla \cdot \left(\left[\frac{\mathrm{d}m}{\mathrm{d}t} - D_\mathrm{r} \vec{\nabla} \right] \Omega(t,\phi,\theta) \right) \quad (19)$$

$$\frac{\mathrm{d}\mathbf{m}}{\mathrm{d}t} = D_\mathrm{r} \mathbf{m} \times \mathbf{h}(t) \times \mathbf{m} \quad (20)$$

where $\mathbf{m} = (\sin\theta\cos\phi, \sin\theta\sin\phi, \cos\theta)$ is a unit vector parallel to the magnetic moment of the particle, $\mathbf{h}(t) = h_0 \cos(\omega t)\hat{\mathbf{z}}$ is the non-dimensional time-dependent field with $\mathbf{h}(t) = m_0\mu_0\mathbf{H}(t)/k_\mathrm{B}T$ and $D_\mathrm{r} = 1/(2\tau_\mathrm{B})$ is the rotational diffusion coefficient. As described in many papers,[46,47] eqn (19) can be transformed by leveraging the symmetry around the z-axis and expanding Ω as a series of time-dependent Legendre polynomials, $\Omega(t,\theta) = \sum a_n(t)P_n(\cos(\theta))$, in order to obtain a system of recurrent ordinary differential equations (ODEs).

$$\frac{2\tilde{\omega}}{n(n+1)} \frac{\mathrm{d}a_n}{\mathrm{d}\tilde{t}} = -a_n + h_0 \cos(\tilde{t}) \cdot \left[\frac{a_{n-1}}{2n-1} - \frac{a_{n+1}}{2n+3} \right] \quad (21)$$

where $\tilde{t} = \omega t$ is a dimensionless time. This equation can be solved numerically by truncating the system ODEs to a given value of n, which means by approximating $a_n = 0 \forall n > n_\mathrm{max}$. Once the system is solved, the magnetization can be computed as:

$$M(t) = \mathcal{N} m_0 \langle \cos(\theta) \rangle = \mathcal{N} m_0 \int_0^\pi \Omega(t,\theta) \cos(\theta) \sin(\theta) \mathrm{d}\theta \quad (22)$$

and using the orthogonality properties of the Legendre polynomials, it can be shown that $M(t) = \frac{2}{3}\mathcal{N} \cdot m_0 \cdot a_1(t)$.

In this work, we have employed the Python ODE solver odeint from the scipy library.[64] The initial conditions that we have employed are $a_0 = 0.5$ which is an imposition from the normalization conditions: $\int_0^\pi \Omega(t,\theta) \cdot \sin(\theta)\mathrm{d}\theta = 1$,

$$a_1 = -\frac{h_0\tilde{\omega}}{2(\tilde{\omega}^2 - 1)} \quad (23)$$

which is the analytical solution when the system is truncated to first order and $a_{n>1} = 0$. To ensure that the calculated cycle has sufficient precision, we first run the solver with a fixed number of differential equations (5 in this case) until the condition $|\max(M(t)) + \min(M(t))| < 10^{-4}$ is satisfied, ensuring that a periodic solution has been reached. Next, we rerun the solver, increasing the number of differential equations by 5, and verify that the relative difference between the areas of the cycles calculated with 5 and 10 equations is smaller than 10^{-5}. If this condition is not met, we further increase the number of equations by 5 and repeat the process iteratively until the relative change in the areas, when increasing the number of equations by 5, is below 10^{-5}. This approach ensures that we always used a sufficient number of equations, regardless of the parameters employed (in general, a higher field intensity requires solving more equations).

Numerical calculation of the area from the time-dependent magnetization

The area of a magnetization cycle can be computed using the integral:

$$\mathcal{A} = \mu_0 \oint M(H)\mathrm{d}H \quad (24)$$

However, since the FPE provides the magnetization as a function of time, it is more convenient to express this integral in terms of time. Using the relationship $\mathrm{d}H = H_0\omega\sin(\omega t)\mathrm{d}t$, the integral transforms into:

$$\mathcal{A} = \mu_0 H_0 \omega \int_0^{1/f} M(t)\sin(\omega t)\mathrm{d}t \quad (25)$$

which, in terms of dimensionless quantities, can be rewritten as:

$$\tilde{\mathcal{A}} = \int_0^{2\pi} \tilde{M}(\tilde{t})\sin(\tilde{t})\mathrm{d}\tilde{t} \quad (26)$$

The integral was then evaluated numerically using the trapezoidal rule.

Fitting algorithm

The relatively large number of fitting parameters revealed that the quality of fits obtained through standard methods was highly dependent on the initial parameter guesses. In many cases, this dependence led to suboptimal or incorrect fits. This reliance on initial parameter estimates underscores a significant limitation: a characterization method loses its practical utility if it requires prior knowledge or an estimation of the system parameters.

To address this issue, we employed a two-step optimization technique. In the first step, a fitting method called parallel tempering[55] was applied, which, starting from random parameters, runs in parallel multiple MC algorithms that minimize a cost function in order to effectively narrow the parameter combination toward the correct solution, regardless of the quality of the initial guesses. Once this method identifies parameters close to the solution, the second step involves applying a Gauss–Newton algorithm (described below). When provided with favorable initial conditions, this algorithm quickly identifies the parameters that best minimize a cost function.

Parallel tempering algorithm

In the parallel tempering algorithm, multiple MC simulations were run in parallel at different MC temperatures, T_MC. In every N_swap steps, we attempt to exchange the parameter sets, $\{\Lambda_i\}$, between simulations at different temperatures, with the swap probability given by:

$$P_\mathrm{swap} = \min\{1, \exp((\beta_{\mathrm{MC},i} - \beta_{\mathrm{MC},j})[\mathcal{C}(\Lambda_i) - \mathcal{C}(\Lambda_j)])\} \quad (27)$$

where $\beta_\mathrm{MC} = 1/T_\mathrm{MC}$ and $\mathcal{C}$ represents the cost function (eqn (18)). For this problem, the loss function used was the sum of

relative error between the experimentally measured area ($A_{\mathrm{exp}}(\xi^{(i)})$) and the predicted area for a given set of parameters ($A(\mathbf{\Lambda},\ \xi^{(i)})$) for each measured area. A detailed explanation of the fitting algorithm can be found in the ESI† and the source code used for the fitting process is available in the following repository.[56]

We employed seven different Monte Carlo temperatures, T_{MC} = 0.0001, 0.0005, 0.001, 0.005, 0.01, 0.05, and 0.1, during the fitting process. To avoid biasing the optimization, we initialized the parameter guesses randomly within broad ranges: $M_{\mathrm{s}}\in[10^4,\ 10^6]$ A m^{-1}, $r_{\mathrm{c}}\in[5,\ 30]$ nm, and $\sigma_{\mathrm{c}}\in[0.05,\ 1]r_{\mathrm{c}}$. The algorithm was run for 5000 consecutive steps and parameter swaps between different MC temperatures were attempted every 200 steps.

Gauss–Newton algorithm

The Gauss–Newton algorithm[65] was used to refine the parameter set $\mathbf{\Lambda}$, which was initially determined using the parallel tempering algorithm. This method iteratively updates the fitting parameters to minimize the sum of the squared residuals, which represent the difference between the model predictions and the experimental values. In our case, since the cost function to be minimized is defined in eqn (18), the residuals are given by:

$$\mathcal{R}_i(\mathbf{\Lambda}) = \sqrt{\frac{\left|A(\mathbf{\Lambda},\ \xi^{(i)}) - A_{\mathrm{exp}}(\xi^{(i)})\right|}{A_{\mathrm{exp}}(\xi^{(i)})}}. \tag{28}$$

During the iterative process, the update of the parameters is based on the Jacobian matrix of the residuals:

$$\mathcal{J}_{ij} = \frac{\partial \mathcal{R}_i(\mathbf{\Lambda})}{\partial \Lambda_j}, \tag{29}$$

which we calculated numerically in each step using finite differences. This Jacobian is then used to update the parameters according to the following expression:

$$\mathbf{\Lambda}^{n+1} = \mathbf{\Lambda}^n - (\mathbf{J}^\top\mathbf{J} + \mathbf{R})^{-1}\mathbf{J}^\top\mathcal{R}(\mathbf{\Lambda}^n), \tag{30}$$

where $\mathbf{R} = 10^{-5}\mathcal{I}$ is a regularization matrix introduced to ensure that $\mathbf{J}^\top\mathbf{J}$ is invertible. The iterative algorithm continues until the norm of the residual vector is smaller than 10^{-5}.

The standard errors of the parameters can be estimated from the covariance matrix:[65]

$$\mathbf{C} = \tau^2(\mathbf{J}^\top\mathbf{J} + \mathbf{R})^{-1} \tag{31}$$

where τ^2 is the variance of the residuals, computed as:

$$\tau^2 = \frac{\|\ \mathcal{R}(\mathbf{\Lambda})\ \|^2}{N_{\mathrm{ex}} - N_{\mathrm{p}}}, \tag{32}$$

with N_{p} being the number of parameters. The standard error of each parameter Λ_j is then:

$$\mathrm{SE}(\Lambda_j) = \sqrt{C_{jj}}. \tag{33}$$

Calculation of the area of distributions of particles

In the experimental measurements, as well as in all the simulations and adjustments we have made, the particles do not all have the same size. Instead, they follow a size distribution with an average size r_{c} and a standard deviation σ_{c}, which is commonly approximated by a log–normal distribution:[57]

$$p(x;\ \tilde{\mu},\ \tilde{\sigma}) = \frac{1}{x\tilde{\sigma}\sqrt{2\pi}}\exp\left(-\frac{(\ln x - \tilde{\mu})^2}{2\tilde{\sigma}^2}\right), \quad x > 0, \tag{34}$$

where the parameters $\tilde{\mu}$ and $\tilde{\sigma}$ are related to the mean and standard deviation of the distribution as follows:

$$\tilde{\mu} = \ln\left(\frac{\mu^2}{\sqrt{\mu^2 + \sigma^2}}\right), \tag{35}$$

$$\tilde{\sigma} = \sqrt{\ln\left(1 + \frac{\sigma^2}{\mu^2}\right)}. \tag{36}$$

In this situation, the experimentally measured area is the sum of the area of each particle's cycle $A = \sum A_i \approx \mathcal{N}\int A(r)p(r;\ r_{\mathrm{c}},\ \sigma_{\mathrm{c}})\mathrm{d}r$. When calculating the total area of a particle system using eqn (1), it is important to note that the area is normalized by m_0, which depends on r_{c}. Therefore, the total area is given by the expression:

$$A(r_{\mathrm{c}},\ \sigma_{\mathrm{c}}) = N\mu_0 H_0 \int_0^\infty \tilde{\mathcal{A}}(r)m_0(r)p(r;\ r_{\mathrm{c}},\ \sigma_{\mathrm{c}})\mathrm{d}r \tag{37}$$

To average and nondimensionalize the area, we divided the total area by $N\mu_0 H_0\langle m_0\rangle$, where

$$\langle m_0\rangle = M_{\mathrm{s}}\int_0^\infty \frac{4}{3}\pi r^3 p(r;\ r_{\mathrm{c}},\ \sigma_{\mathrm{c}})\mathrm{d}r \tag{38}$$

To obtain the dimensionless average area, we divided eqn (37) by eqn (38), arriving at:

$$\langle\tilde{\mathcal{A}}\rangle(r_{\mathrm{c}},\ \sigma_{\mathrm{c}}) = \frac{\int_0^\infty \tilde{\mathcal{A}}(r)r^3 p(r;\ r_{\mathrm{c}}\,\sigma_{\mathrm{c}})\mathrm{d}r}{\int_0^\infty r^3 p(r;\ r_{\mathrm{c}}\,\sigma_{\mathrm{c}})\mathrm{d}r} \tag{39}$$

To calculate this integral, we used the "gsl_integration_qagiu" method from the GNU Scientific Library[66] in C++. This method allows the evaluation of integrals over a semi-infinite space by applying a change of variables that transforms the integration domain into [0, 1]. After this transformation, an adaptive algorithm is used to compute the integral with the desired accuracy.

Numerical simulation of the AC magnetization cycles

To simulate the hysteresis cycles, we assumed a sufficiently diluted regime where the magnetic and hydrodynamic interactions between the magnetic nanoparticles (MNPs) are negligible. As a result, we only need to account for the rotational

motion of the particles, while their translational motion can be disregarded. The rotational motion is considered within the overdamped regime, where the torque exerted by the external magnetic field on particle i, given by $\mathbf{T}_M{}^i = \mu_0 m_0{}^i \mathbf{u}_m \times \mathbf{H}(t)$, is balanced by the viscous torque from the surrounding fluid $\mathbf{T}^i_{vis} = -\xi_r \dot{\theta}^i$, along with the stochastic torque arising from random collisions between the solvent molecules and the particles.

This approximation is valid because the relaxation time for rotational inertia, $\tau_r = I/\xi_r \approx 1$ ps (where I is the moment of inertia of the particles and $\xi_r = 8\pi\eta r_h{}^3$ is the rotational friction coefficient), is much smaller than the period of the AC cycles, $1/f \approx$10–100 μs. The balance of torques leads to the following equation of motion:

$$\dot{\theta} = \frac{\mathbf{T}_M}{\xi_r} + \sqrt{\frac{2k_B T}{\xi_r}}\mathcal{W} \tag{40}$$

where $\mathcal{W}$ is a vector of independent Wiener increments consisting of three random components with zero mean and unit variance. To solve this stochastic differential equation, the Euler–Maruyama algorithm was employed, as detailed in ref. 67 and further described in ref. 68.

The algorithm was implemented using the GPU-based software UAMMD[42] simulating the Brownian motion of 10^5 particles for each experiment.

A crucial aspect of the simulation is the choice of initial orientations, as these determine how many cycles are required for the particles to reach the equilibrium trajectory. This is especially important when the parameters place the system in the linear regime, where many cycles (more than 1000 in some cases) may be necessary for the system to reach the equilibrium cycle starting from a condition where all particles are either randomly oriented or aligned in the same direction.

In contrast, when the system is outside the linear regime, the initial conditions are not as significant, since the equilibrium trajectory is reached after only a few cycles. For this reason, whenever possible, we initialized the particles according to the orientation distribution expected from the FPE in the linear regime at $t = 0$:

$$\Omega(0, \cos(\theta)) = \frac{1}{2} + \frac{\tilde{\omega} h_0}{2(\tilde{\omega}^2 - 1)}\cos(\theta) \tag{41}$$

This result is obtained by solving eqn (21), truncating it for $n > 1$, such that $\Omega(t, \cos(\theta)) = a_0 + a_1(t)\cos(\theta)$. As explained earlier, we know that $a_0 = 1/2$ and to calculate a_1, we propose the solution $a_1 = S\cdot\sin(\omega t) + C\cdot\cos(\omega t)$, and then the coefficients S and C were calculated.

It is important to note that when $\frac{\tilde{\omega} h_0}{2(\tilde{\omega}^2 - 1)} \geq 1/2$, eqn (41) is no longer valid, as it leads to negative probabilities. In such cases, the particles are initially aligned with the z-axis.

To ensure that the system has reached the equilibrium trajectory, the simulation was run for 500 magnetization cycles.

Magnetic nanoparticles

The MNPs employed in this study are commercial magnetite nanoflowers (cobalt ferrite, references 123-00-301 and 124-02-501, respectively, manufactured by Micromod Nanopartikel GmbH, Germany) with uncoated (plain) and dextran-coated surfaces functionalized with carboxylic groups.

Experimental methods: AC magnetometry

AC magnetometry measurements were performed using commercial inductive magnetometers (SENS and ADVANCE AC Hyster™ Series, Nanotech Solutions, Spain) to study the AC magnetization cycles of suspensions of cobalt ferrite MNPs synthesised by Micromod. The particle concentration in each suspension was 40 μg_{Fe+Co} L^{-1} and all measurements were conducted at room temperature (~25 °C). The magnetization cycles were recorded three times for each measurement and the average cycle was used to compute the AC magnetic hysteresis area and its associated error, which was consistently very small.

Preparation of magnetic suspensions dispersed in media with different viscosities

Six suspensions of 100 microliters each were prepared, in which the commercial magnetite nanoflowers mentioned above were dispersed in double-distilled water solutions containing varying fractions of glycerol (0, 15, 32, and 45%). The iron content was maintained at 1 g of Fe and Co per liter in all viscous suspensions.

Preparation of bioconjugated MNPs

Magnetic nanoparticles (MNPs) were functionalized with a specific peptide sequence, GST-MEEVF,[69] which is recognized by the engineered TPR domain TPR-MMY[70] and used as a target monovalent analyte. For the bioconjugation of MNP formulations, the carboxylic groups present in the dextran coating of the particles were utilized.

Before conjugation, these carboxylic groups needed to be activated. To achieve this, 1 mL of MNPs at a concentration of 2.5 g_{Fe+Co} L^{-1} was incubated for 4 hours at 37 °C with 150 mmol of NHS and 150 mmol of EDC per gram of Fe + Co. Following activation, the MNP suspension was washed using centrifugal filters (Amicon Ultra) with a molecular weight cut-off (MWCO) of 100 kDa.

The activated MNPs were then redispersed in 10 mM sodium phosphate buffer at pH 7.4 to a final volume of 1 mL, with the filtration process repeated three times. Once the carboxylic groups were activated, the MNPs were incubated overnight at 37 °C at a concentration of 2.5 g_{Fe+Co} L^{-1} with 100 μL

of 167 μM GST-MEEVF fusion protein in phosphate buffer (PB). Finally, the functionalized MNPs were purified by gel filtration through a Sepharose 6 CLB column using PB.

Author contributions

This project was conceived and designed by R. D.-B., F. J. T. and P. P.-A. Experiments were directed by F. J. T. and performed by M. M.-S., S. O.-O. and E. S. D. Theory and simulations were directed by R. D.-B. and developed by P. P.-A. The manuscript was written by P. P.-A. and R. D.-B. and revised by F. J. T.

Data availability

Data for this article, including measurement data, and the automated-searching codes are available at **https://github.com/PabloPalaciosAlonso/ACMHystBrown.git**.

Conflicts of interest

The authors declare no financial, direct, or indirect competing interests in the research and preparation of this paper.

Acknowledgements

The authors acknowledge funding from Comunidad de Madrid (Mag4TIC, TEC-2024/TEC-380) and the Spanish Research Agency through projects PID2020-117080RB-C51, PID2020-117080RB-C53, and PCI2019-103600 and through the Prueba de Concepto Project PDC2021-121441-C21. PPA thanks Comunidad de Madrid for funding his contract under project PEJ-2020-AI/IND-19394. Furthermore, this work was funded by the STRIKE ETN Marie Curie Action, Horizon Europe Program (grant agreement no. 101072462).

References

1 M. Meléndez, A. Vázquez-Quesada and R. Delgado-Buscalioni, Load Impedance of Immersed Layers on the Quartz Crystal Microbalance: A Comparison with Colloidal Suspensions of Spheres, *Langmuir*, 2020, **36**, 9225–9234.
2 D. Martin-Jimenez, E. Chacon, P. Tarazona and R. Garcia, Atomically resolved three-dimensional structures of electrolyte aqueous solutions near a solid surface, *Nat. Commun.*, 2016, **7**, 12164.
3 A. Giustini, A. Petryk, S. Cassim, J. Tate, I. Baker and P. Hoopes, MAGNETIC NANOPARTICLE HYPERTHERMIA IN CANCER TREATMENT, *Nano LIFE*, 2010, **1**, 17–32.
4 H. Gavilán, S. K. Avugadda, T. Fernández-Cabada, N. Soni, M. Cassani, B. T. Mai, R. Chantrell and T. Pellegrino, Magnetic nanoparticles and clusters for magnetic hyperthermia: optimizing their heat performance and developing combinatorial therapies to tackle cancer, *Chem. Soc. Rev.*, 2021, **50**, 11614–11667.
5 C. Yadel, A. Michel, S. Casale and J. Fresnais, Hyperthermia Efficiency of Magnetic Nanoparticles in Dense Aggregates of Cerium Oxide/Iron Oxide Nanoparticles, *Appl. Sci.*, 2018, **8**, 1241.
6 J. Liu, B. Jang, D. Issadore and A. Tsourkas, Use of magnetic fields and nanoparticles to trigger drug release and improve tumor targeting, *Wiley Interdiscip. Rev.: Nanomed. Nanobiotechnol.*, 2019, **11**, e1571.
7 E. Kianfar, Magnetic Nanoparticles in Targeted Drug Delivery: a Review, *J. Supercond. Novel Magn.*, 2021, 1709–1735.
8 A. Meffre, B. Mehdaoui, V. Connord, J. Carrey, P. F. Fazzini, S. Lachaize, M. Respaud and B. Chaudret, Complex Nano-objects Displaying Both Magnetic and Catalytic Properties: A Proof of Concept for Magnetically Induced Heterogeneous Catalysis, *Nano Lett.*, 2015, **15**, 3241–3248.
9 A. Gallo-Cordova, J. J. Castro, E. L. Winkler, E. Lima, R. D. Zysler, M. del Puerto Morales, J. G. Ovejero and D. A. Streitwieser, Improving degradation of real wastewaters with self-heating magnetic nanocatalysts, *J. Cleaner Prod.*, 2021, **308**, 127385.
10 M. Colombo, S. Carregal-Romero, M. F. Casula, L. Gutiérrez, M. P. Morales, I. B. Böhm, J. T. Heverhagen, D. Prosperi and W. J. Parak, Biological applications of magnetic nanoparticles, *Chem. Soc. Rev.*, 2012, **41**, 4306–4334.
11 L. Wu, Y. Zhang, G. Steinberg, H. Qu, S. Huang, M. Cheng, T. Bliss, F. Du, J. Rao, G. Song, L. Pisani, T. Doyle, S. Conolly, K. Krishnan, G. Grant and M. Wintermark, A Review of Magnetic Particle Imaging and Perspectives on Neuroimaging, *Am. J. Neuroradiol.*, 2019, **40**, 206–212.
12 P. Szwargulski, M. Wilmes, E. Javidi, F. Thieben, M. Graeser, M. Koch, C. Gruettner, G. Adam, C. Gerloff, T. Magnus, T. Knopp and P. Ludewig, Monitoring Intracranial Cerebral Hemorrhage Using Multicontrast Real-Time Magnetic Particle Imaging, *ACS Nano*, 2020, **14**, 13913–13923.
13 S. Ota, H. Kosaka, K. Honda, K. Hoshino, H. Goto, M. Futagawa, Y. Takemura and K. Shimizu, Characterization of Microscopic Structures in Living Tumor by In Vivo Measurement of Magnetic Relaxation Time Distribution of Intratumor Magnetic Nanoparticles, *Adv. Mater.*, 2024, **36**, 2404766.
14 X. Feng, G. Jia, J. Peng, L. Huang, X. Liang, H. Zhang, Y. Liu, B. Zhang, Y. Zhang, M. Sun, P. Li, Q. Miao, Y. Wang, L. Xi, K. Hu, T. Li, H. Hui and J. Tian, Relaxation spectral analysis in multi-contrast vascular magnetic particle imaging, *Med. Phys.*, 2023, **50**, 4651–4663.
15 J. Connolly and T. G. St Pierre, Proposed biosensors based on time-dependent properties of magnetic fluids, *J. Magn. Magn. Mater.*, 2001, **225**, 156–160.
16 K. Enpuku, T. Tanaka, Y. Tamai and M. Matsuo, AC susceptibility of magnetic markers in suspension for liquid phase immunoassay, *J. Magn. Magn. Mater.*, 2009, **321**, 1621–1624.
17 K. Enpuku, Y. Tsujita, K. Nakamura, T. Sasayama and T. Yoshida, Biosensing utilizing magnetic markers and

superconducting quantum interference device, *Supercond. Sci. Technol.*, 2017, **30**, 053002.

18 J.-J. Chieh, W.-C. Wei, S.-H. Liao, H.-H. Chen, Y.-F. Lee, F.-C. Lin, M.-H. Chiang, M.-J. Chiu, H.-E. Horng and S.-Y. Yang, Eight-Channel AC Magnetosusceptometer of Magnetic Nanoparticles for High-Throughput and Ultra-High-Sensitivity Immunoassay, *Sensors*, 2018, **18**, 1043.

19 S. Balaban Hanoglu, D. Harmanci, N. Ucar, S. Evran and S. Timur, Recent Approaches in Magnetic Nanoparticle-Based Biosensors of miRNA Detection, *Magnetochemistry*, 2023, **9**, 23.

20 Z. Du, Y. Cui, Y. Sun, H. Zhang, S. Bai and T. Yoshida, Empirical Expression of AC Susceptibility of Magnetic Nanoparticles and Potential Application in Biosensing, *IEEE Trans. NanoBiosci.*, 2022, **21**, 496–501.

21 J. Zhong, E. Rösch, T. Viereck and M. Schilling, Toward Rapid and Sensitive Detection of SARS-CoV-2 with Functionalized Magnetic Nanoparticles, *ACS Sens.*, 2021, **6**, 976–984.

22 E. Sanz-de Diego, A. Aires, P. Palacios-Alonso, D. Cabrera, N. Silvestri, C. C. Vequi-Suplicy, E. J. Artés-Ibáñez, J. Requejo-Isidro, R. Delgado-Buscalioni, T. Pellegrino, A. L. Cortajarena and F. J. Terán, Multiparametric modulation of magnetic transduction for biomolecular sensing in liquids, *Nanoscale*, 2024, **16**, 4082–4094.

23 J. Carrey, B. Mehdaoui and M. Respaud, Simple models for dynamic hysteresis loop calculations of magnetic single-domain nanoparticles: Application to magnetic hyperthermia optimization, *J. Appl. Phys.*, 2011, **109**, 083921.

24 Y. Sun, Z. Du, Z. Haochen, W. Haozhe, T. Sasayama and T. Yoshida, Simultaneous Estimation of Magnetic Moment and Brownian Relaxation Time Distributions of Magnetic Nanoparticles Based on Magnetic Particle Spectroscopy for Biosensing Application, *Nanoscale*, 2023, **15**, 16089–16102.

25 W. I. Goldburg, Dynamic light scattering, *Am. J. Phys.*, 1999, **67**, 1152–1160.

26 A. Malloy and B. Carr, NanoParticle Tracking Analysis – The Halo™ System, *Part. Part. Syst. Charact.*, 2006, **23**, 197–204.

27 S. P. Yeap, Characterization of magnetic nanoparticle by dynamic light scattering, *Nanoscale Res. Lett.*, 2013, **8**, 1–14.

28 S. Yahata, M. Hirose, T. Ueno, H. Nagumo and K. Sakai-Kato, Effect of Sample Concentration on Nanoparticle Tracking Analysis of Small Extracellular Vesicles and Liposomes Mimicking the Physicochemical Properties of Exosomes, *Chem. Pharm. Bull.*, 2021, **69**, 1045–1053.

29 E. Serrano-Pertierra, M. Oliveira-Rodríguez, M. Matos, G. Gutierrez, A. Moyano, M. Salvador, M. Rivas and M. C. Blanco-López, Extracellular Vesicles: Current Analytical Techniques for Detection and Quantification, *Biomolecules*, 2020, **10**, 824.

30 A. Fornara, P. Johansson, K. Petersson, S. Gustafsson, J. Qin, E. Olsson, D. Ilver, A. Krozer, M. Muhammed and C. Johansson, Tailored Magnetic Nanoparticles for Direct and Sensitive Detection of Biomolecules in Biological Samples, *Nano Lett.*, 2008, **8**, 3423–3428.

31 P. Debye, Polar molecules. By P. Debye, Ph.D., Pp. 172. New York: Chemical Catalog Co., Inc., 1929. $ 3.50, *J. Soc. Chem. Ind.*, 1929, **48**, 1036–1037.

32 A. Prieto Astalan, C. Jonasson, K. Petersson, J. Blomgren, D. Ilver, A. Krozer and C. Johansson, Magnetic response of thermally blocked magnetic nanoparticles in a pulsed magnetic field, *J. Magn. Magn. Mater.*, 2007, **311**, 166–170.

33 F. Ludwig, E. Heim and M. Schilling, Characterization of magnetic core–shell nanoparticles by fluxgate magnetorelaxometry, ac susceptibility, transmission electron microscopy and photon correlation spectroscopy—A comparative study, *J. Magn. Magn. Mater.*, 2009, **321**, 1644–1647.

34 F. Ludwig, A. Guillaume, M. Schilling, N. Frickel and A. M. Schmidt, Determination of core and hydrodynamic size distributions of CoFe2O4 nanoparticle suspensions using ac susceptibility measurements, *J. Appl. Phys.*, 2010, **108**, 033918.

35 R. M. Ferguson, A. P. Khandhar, C. Jonasson, J. Blomgren, C. Johansson and K. M. Krishnan, Size-Dependent Relaxation Properties of Monodisperse Magnetite Nanoparticles Measured Over Seven Decades of Frequency by AC Susceptometry, *IEEE Trans. Magn.*, 2013, **49**, 3441–3444.

36 F. Ludwig, H. Remmer, C. Kuhlmann, T. Wawrzik, H. Arami, R. M. Ferguson and K. M. Krishnan, Self-consistent magnetic properties of magnetite tracers optimized for magnetic particle imaging measured by ac susceptometry, magnetorelaxometry and magnetic particle spectroscopy, *J. Magn. Magn. Mater.*, 2014, **360**, 169–173.

37 S. Bogren, A. Fornara, F. Ludwig, M. Del Puerto Morales, U. Steinhoff, M. F. Hansen, O. Kazakova and C. Johansson, Classification of Magnetic Nanoparticle Systems—Synthesis, Standardization and Analysis Methods in the NanoMag Project, *Int. J. Mol. Sci.*, 2015, **16**, 20308–20325.

38 K. K. Narayanasamy, M. Cruz-Acuña, C. Rinaldi, J. Everett, J. Dobson and N. D. Telling, Alternating current (AC) susceptibility as a particle-focused probe of coating and clustering behaviour in magnetic nanoparticle suspensions, *J. Colloid Interface Sci.*, 2018, **532**, 536–545.

39 K. Wu, V. Chugh, V. Dk, A. di Girolamo, Y. Wang, R. Saha, S. Liang, M. Cheeran and J.-P. Wang, One-step, Wash-free, Nanoparticle Clustering-based Magnetic Particle Spectroscopy (MPS) Bioassay Method for Detection of SARS-CoV-2 Spike and Nucleocapsid Proteins in Liquid Phase, *ACS Appl. Mater. Interfaces*, 2021, 44136–44146.

40 P. Palacios-Alonso, E. Sanz-de Diego, R. P. Peláez, A. L. Cortajarena, F. J. Teran and R. Delgado-Buscalioni, Predicting the size and morphology of nanoparticle clusters driven by biomolecular recognition, *Soft Matter*, 2023, **19**, 8929–8944.

41 T. Yoshida, K. Ogawa, K. Enpuku, N. Usuki and H. Kanzaki, AC Susceptibility of Magnetic Fluid in Nonlinear Brownian Relaxation Region: Experiment and Comparison with Numerical Simulation, *Jpn. J. Appl. Phys.*, 2010, **49**, 053001–053007.

42 R. P. Peláez, P. Ibáñez-Freire, P. Palacios-Alonso, A. Donev and R. Delgado-Buscalioni, Universally Adaptable

Multiscale Molecular Dynamics (UAMMD). A native-GPU software ecosystem for complex fluids, soft matter, and beyond, *Comput. Phys. Commun.*, 2025, **306**, 109363.
43 M. Wolfschwenger, A. Jaufenthaler, F. Hanser, J. Gamper, T. S. Hofer and D. Baumgarten, Molecular dynamics modelling of interacting magnetic nanoparticles for investigating equilibrium and dynamic ensemble properties, *Appl. Math. Modell.*, 2024, **136**, 115624.
44 W. T. Coffey, P. J. Cregg and Y. U. P. Kalmykov, in *On the Theory of Debye and Néel Relaxation of Single Domain Ferromagnetic Particles*, John Wiley & Sons, Ltd, 1992, pp. 263–464.
45 Y. L. Raikher and V. I. Stepanov, in *Nonlinear Dynamic Susceptibilities and Field-Induced Birefringence in Magnetic Particle Assemblies*, John Wiley & Sons, Ltd, 2004, ch. 4, pp. 419–588.
46 R. J. Deissler, Y. Wu and M. A. Martens, Dependence of Brownian and Néel relaxation times on magnetic field strength, *Med. Phys.*, 2014, **41**, 012301.
47 D. B. Reeves and J. B. Weaver, Approaches for modeling magnetic nanoparticle dynamics, *Crit. Rev. Biomed. Eng.*, 2014, **42**, 85–93.
48 A. A. Kuznetsov and A. F. Pshenichnikov, Nonlinear response of a dilute ferrofluid to an alternating magnetic field, *J. Mol. Liq.*, 2022, **346**, 117449.
49 H. Zhang, B. Zhang, X. Feng, Y. Zhang, Y. Chen, H. Hui and J. Tian, Rapid Viscosity Measurement Using Arbitrary Frequency Magnetic Particle Spectrometer, *IEEE Trans. Instrum. Meas.*, 2023, **72**, 1–10.
50 J. Zhong, M. Schilling and F. Ludwig, Magnetic nanoparticle thermometry independent of Brownian relaxation, *J. Phys. D: Appl. Phys.*, 2018, **51**, 015001.
51 Z. Du, G. Zhao, Z. Hua, N. Ye, Y. Sun, W. Wu, Z. Haochen, L. Yu, S. Han, W. Haozhe, W. Liu and T. Yoshida, A Novel Estimation Method for Temperature of Magnetic Nanoparticles Dominated by Brownian Relaxation Based on Magnetic Particle Spectroscopy, *IEEE Trans. Instrum. Meas.*, 2024, 1.
52 J. Zhong, M. Schilling and F. Ludwig, Simultaneous Imaging of Magnetic Nanoparticle Concentration, Temperature, and Viscosity, *Phys. Rev. Appl.*, 2021, **16**, 054005.
53 J. Liu, Z. Zhang, Q. Xie and W. Liu, Dual-phase model: Estimating the temperature and hydrodynamic size of magnetic nanoparticles with protein-corona formation, *Appl. Phys. Lett.*, 2024, **124**, 092408.
54 N.-S. Cheng, Formula for the Viscosity of a Glycerol-Water Mixture, *Ind. Eng. Chem. Res.*, 2008, **47**, 3285–3288.
55 D. J. Earl and M. W. Deem, Parallel tempering: Theory, applications, and new perspectives, *Phys. Chem. Chem. Phys.*, 2005, **7**, 3910–3916.
56 P. Palacios-Alonso, ACMHystBrow, 2024, **https://github.com/PabloPalaciosAlonso/ACMHystBrown.git**.
57 R. Chantrell, J. Popplewell and S. Charles, Measurements of particle size distribution parameters in ferrofluids, *IEEE Trans. Magn.*, 1978, **14**, 975–977.
58 E. Sanz de Diego, Ph.D. thesis, Universidad Autónoma de Madrid, 2022.
59 S. R. Mokhosi, W. Mdlalose, A. Nhlapo and M. Singh, Advances in the Synthesis and Application of Magnetic Ferrite Nanoparticles for Cancer Therapy, *Pharmaceutics*, 2022, **14**, 937.
60 J. Gross, S. Sayle, A. R. Karow, U. Bakowsky and P. Garidel, Nanoparticle tracking analysis of particle size and concentration detection in suspensions of polymer and protein samples: Influence of experimental and data evaluation parameters, *Eur. J. Pharm. Biopharm.*, 2016, **104**, 30–41.
61 O. Snyder, A. Campbell, L. Christenson and M. Weiss, Improving Reproducibility to Meet Minimal Information for Studies of Extracellular Vesicles 2018 Guidelines in Nanoparticle Tracking Analysis, *J. Visualized Exp.*, 2021, E63059.
62 C. D. Cabrera, T. A. Aires. I. E. J. Artes, D. D. J. Camarero, C. A. Lopez, F. J. Teran, Method for Detection of an Analyte. Patent US20200284787A1, 2020, Filing date: 2018-11-08, Application number: US16/762,851.
63 P. Rodríguez-Sevilla, F. Sanz-Rodríguez, R. P. Peláez, R. Delgado-Buscalioni, L. Liang, X. Liu and D. Jaque, Upconverting Nanorockers for Intracellular Viscosity Measurements During Chemotherapy, *Adv. Biosyst.*, 2019, **3**, 1900082.
64 P. Virtanen, R. Gommers, T. E. Oliphant, M. Haberland, T. Reddy, D. Cournapeau, E. Burovski, P. Peterson, W. Weckesser, J. Bright, S. J. van der Walt, M. Brett, J. Wilson, K. J. Millman, N. Mayorov, A. R. J. Nelson, E. Jones, R. Kern, E. Larson, C. J. Carey, İ. Polat, Y. Feng, E. W. Moore, J. VanderPlas, D. Laxalde, J. Perktold, R. Cimrman, I. Henriksen, E. A. Quintero, C. R. Harris, A. M. Archibald, A. H. Ribeiro, F. Pedregosa, P. van Mulbregt and SciPy 1.0 Contributors, SciPy 1.0: Fundamental Algorithms for Scientific Computing in Python, *Nat. Methods*, 2020, **17**, 261–272.
65 D. M. Bates and D. G. Watts, *Nonlinear Regression Analysis and Its Applications*, John Wiley & Sons, Inc., New York, 1988.
66 B. Gough, *GNU scientific library reference manual*, Network Theory Ltd., 2009.
67 P. Kloeden and E. Platen, *The Numerical Solution of Stochastic Differential Equations*, Springer Berlin, Heidelberg, 1992, vol. 23.
68 S. Delong, F. Balboa Usabiaga and A. Donev, Brownian dynamics of confined rigid bodies, *J. Chem. Phys.*, 2015, **143**, 144107.
69 M. E. Jackrel, R. Valverde and L. Regan, Redesign of a protein–peptide interaction: Characterization and applications, *Protein Sci.*, 2009, **18**, 762–774.
70 R. P. Ilagan, E. Rhoades, D. F. Gruber, H.-T. Kao, V. A. Pieribone and L. Regan, A new bright green-emitting fluorescent protein – engineered monomeric and dimeric forms, *FEBS J.*, 2010, **277**, 1967–1978.